

Altered expression of Presenilin2 impacts endolysosomal homeostasis and synapse function in Alzheimer's disease-relevant brain circuits

Received: 15 March 2024

Accepted: 21 November 2024

Published online: 29 November 2024

 Check for updates

Anika Perdok ^{1,2}, Zoë P. Van Acker ^{1,2,7}, Céline Vrancx ^{1,2,7},
Ragna Sannerud ^{1,2}, Inge Vorsters ^{1,2}, Assunta Verrengia^{1,2},
Zsuzsanna Callaerts-Végh ³, Eline Creemers⁴, Sara Gutiérrez Fernández^{2,5},
Britt D'hauw⁴, Lutgarde Serneels^{2,6}, Keimpe Wierda⁴,
Lucía Chávez-Gutiérrez ^{2,5} & Wim Annaert ^{1,2} 

Rare mutations in the gene encoding presenilin2 (PSEN2) are known to cause familial Alzheimer's disease (FAD). Here, we explored how altered PSEN2 expression impacts on the amyloidosis, endolysosomal abnormalities, and synaptic dysfunction observed in female APP knock-in mice. We demonstrate that PSEN2 knockout (KO) as well as the FAD-associated N141IKI mutant accelerate AD-related pathologies in female mice. Both models showed significant deficits in working memory that linked to elevated PSEN2 expression in the hippocampal CA3 region. The mossy fiber circuit of APPxPSEN2KO and APPxFADPSEN2 mice had smaller pre-synaptic compartments, distinct changes in synaptic vesicle populations and significantly impaired long term potentiation compared to APPKI mice. At the cellular level, altered PSEN2 expression resulted in endolysosomal defects and lowered surface expression of synaptic proteins. As PSEN2/ γ -secretase is restricted to late endosomes/lysosomes, we propose PSEN2 impacts endolysosomal homeostasis, affecting synaptic signaling in AD-relevant vulnerable brain circuits; which could explain how mutant PSEN2 accelerates AD pathogenesis.

γ -Secretases are intramembrane proteases that act as proteolytic switches in various physiological processes through the targeting of a broad range of substrates^{1,2}. They are extensively studied^{3–5} in the context of Alzheimer's disease (AD) where they target the amyloid precursor protein (APP)^{3,6}. γ -Secretases are tetrameric complexes where presenilin (PSEN1 or PSEN2) provides the catalytic activity and nicastrin (NCSTN), anterior pharynx defective 1 (APH1A or B) and

presenilin enhancer 2 (PSENEN2) are essential subunits^{7–9}. The different isoforms of APH1 and PSEN give rise to four distinct complexes¹⁰. After APP ectodomain shedding by β -secretase (BACE1), γ -secretases release the APP intracellular domain (AICD), followed by progressive C-terminal trimming releasing amyloid β (A β) peptides of varying lengths^{11–13}. Mutations in the *APP*, *PSEN1* and *PSEN2* genes cause rare autosomal dominant familial AD (FAD) centralizing γ -secretase and

¹Laboratory for Membrane Trafficking, VIB Center for Brain and Disease Research, Leuven, Belgium. ²Department of Neurosciences, KU Leuven, Herestraat 49box 602, Leuven, Belgium. ³mINT Animal Behavior Facility, Faculty of Psychology, KU Leuven, Tiensestraat 102, Leuven, Belgium. ⁴Electrophysiology Expertise Unit, VIB-Center for Brain and Disease Research, Leuven, Belgium. ⁵Laboratory of Proteolytic Mechanisms mediating Neurodegeneration, Leuven, Belgium. ⁶Mouse Expertise Unit, VIB-Center for Brain and Disease Research, Leuven, Belgium. ⁷These authors contributed equally: Zoë P. Van Acker, Céline Vrancx. ✉e-mail: wim.annaert@kuleuven.be

APP processing in AD, as originally theorized in the amyloid cascade hypothesis^{14,15}. Pathogenic mutations destabilize γ -secretase-substrate interactions, leading to longer, aggregation-prone A β peptides¹², the major constituents of amyloid plaques observed in AD brains.

AD research has predominantly focused on PSEN1/ γ -secretase due to the far more abundant pathogenic mutations found in its gene⁹ and that PSEN1 knock-out (KO) is embryonic lethal^{16,17}. PSEN2KO mice develop normally, with only a minor pulmonary phenotype^{18,19}. However, knocking out PSEN2 in a PSEN1KO model puts forward embryonic lethality²⁰. Post-embryonic full knock out of γ -secretase, obtained by conditionally knocking out all three A β 1 isoforms, results in C-terminal fragment (CTF) accumulation of various substrates, neurodegeneration and neuroinflammation²¹, underscoring a central role for γ -secretase in these processes. Studies in PSEN1 and PSEN2 double KO linked γ -secretase to tau phosphorylation, axonal transport, learning and memory, neurodegeneration and impaired synaptic plasticity^{22–26}, though individual complex contributions remained understudied. Notably, compared to PSEN1, FAD causing mutations in PSEN2 have a later age of onset²⁷ and largely shift processing towards the A β 42 lineage^{28,29}; PSEN1 mutations have a broader range of effects on A β profiles³⁰.

Clear molecular differences between PSEN1 and PSEN2 complexes were recently brought up through the discovery of a unique acidic-dileucine sorting motif that targets PSEN2-complexes to late endosomes and lysosomes (LE/Lys)^{29,31}. As PSEN1/ γ -secretases are more broadly distributed at the cell surface and in (recycling) endosomes, this results in overall complex-selective substrate pools. For instance, PSEN2KO impairs melanosome maturation by failing to process tyrosinase-related protein (TRP1) and premelanosome protein (PMEL)-CTFS²⁹. PSEN2/ γ -secretase also generates intracellular A β (iA β) in LE/Lys²⁹, a highly toxic pool that surges in early stages of the disease, preceding plaque deposition and correlating with synaptic deficits^{32–35}. A β 42, in particular, accumulated in multivesicular bodies (MVBs) (also referred to as LE), wherein the acidic environment strongly accelerated amyloid fibril formation^{36–38} affecting LE/Lys integrity and representing an early event of A β pathogenesis^{39,40}. However, much of this knowledge is based on in vitro studies of aggregation kinetics or cellular uptake of exogenously administered recombinant A β peptides. As PSEN2/ γ -secretase significantly contributes to iA β accumulation in LE/Lys, in vitro and in vivo models with altered PSEN2 expression can now be used to more directly study the impact of iA β . Given its LE/Lys localization, we hypothesized that changes in PSEN2 function, through KO or FAD-linked mutations, may affect A β pathogenesis, potentially through altering iA β and APP-CTF levels. FAD-linked PSEN2 mutants impair intracellular Ca²⁺ stores⁴¹ and are linked to decreased Rab7 recruitment on autophagosomes, connecting Ca²⁺ signaling to autophagy and degradation⁴². Endolysosomal abnormalities appear early in disease as has been shown in murine AD models^{43,44} and patient brain samples⁴⁵. Neurons, being post-mitotic polarized cells, rely heavily on the endolysosomal system to remove dysfunctional organelles and aggregated proteins next to cargo trafficking^{46,47}.

To address how PSEN2 contributes to AD pathogenesis, we crossed APPKI mice with a PSEN2KO or a CRISPR/Cas9 engineered PSEN2 KI mouse harboring the FAD-linked N141I mutation²⁸. In both models, AD-related amyloid pathology, including dystrophic neurites, appeared accelerated along with cognitive defects in the working memory. Notably, long-term potentiation (LTP) was impaired in the hippocampal CA3 region, correlating with morphological changes in mossy-fiber pyramidal neuron synapses. Primary hippocampal neuron data further imply a role for PSEN2 in endolysosomal homeostasis, disruption of which impacts synaptic functioning and circuitry, unveiling molecular mechanisms that may become distorted particularly in FAD-associated PSEN2 variants.

Results

PSEN2 knockout and FADPSEN2 differently affect plaque pathology and A β profiles

Given its role in generating neurotoxic iA β , we hypothesized that altering PSEN2 expression in vivo, through KO or introducing a FAD-mutation, would have opposing effects on AD pathogenesis due to the changes in the iA β pool. We used CRISPR/Cas9 editing to introduce the PSEN2 Volga mutation in C57black6j mice (Figure S1a) by converting asparagine at position 141 to isoleucine, the most prevalent PSEN2 FAD mutation^{27,28} known to shift iA β production to longer more aggregation-prone species²⁹. We created, as such, homozygous mutant mice with the N141I point mutation, as confirmed by PCR (Figure S1a, b) and Sanger sequencing (Figure S1c). These mice, which show no overt phenotypic differences, have higher endogenous mutant PSEN2 levels (Figure S1d), suggesting more stable PSEN2/ γ -secretase levels or a broader distribution. FADPSEN2 and PSEN2KO mice¹⁸ were crossed with the APP NL-G-F KI (APPKI) AD model to investigate AD pathology (hereafter referred to APPxPSEN2KO and APPxFADPSEN2)⁴⁸.

We previously demonstrated that PSEN2/ γ -secretase activity in LE/Lys strongly determined the iA β pool, with FAD mutations shifting this pool towards longer A β 42²⁹. To confirm this, we analyzed conditioned media and cell extracts from primary hippocampal neurons derived from these models. APPxFADPSEN2 neurons showed increased total iA β , whereas this pool is decreased in APPxPSEN2KO (Fig. 1a, b). Secreted A β was correspondingly decreased in APPxFADPSEN2 and increased in APPxPSEN2KO (Fig. 1c), likely due to the absence of PSEN2 driving APP processing to PSEN1/ γ -secretase, and increasing the secreted pool. PSEN1 expression remained stable over time, whereas PSEN2 levels increased with maturing neurons, further augmenting iA β , and underlining PSEN2's role in iA β generation (Fig. 1a). Next, using MesoScale Discovery (MSD) ELISA, we quantified the relative levels of A β 37, A β 38, A β 40 and A β 42 in intracellular and secreted pools. As expected¹², the PSEN2 N141I mutation significantly increased relative A β 42 levels and A β 42:40 ratio (Fig. 1d–g), indicating decreased processivity. In contrast, PSEN2KO in the APPKI background shifted the A β profile to shorter peptides, with significant increased A β 38 and decreased A β 42:40 ratio, reflecting PSEN1 processivity (Fig. 1d–g). Similar results were observed in brain extracts: no differences were seen in the insoluble fraction (Figure S1e), but soluble extracts at 6 months of age showed increased A β 38 and A β 42 for APPxPSEN2KO and APPxFADPSEN2, respectively (Fig. 1h), consistent with altered γ -secretase processivity and 42:40 ratio (Fig. 1 i, j).

Next, we examined how altered A β profiles impacted amyloid pathology, using thioflavin-S positive area as a readout. To note, wild-type mice were not included in these analyses as they do not develop amyloid pathology⁴⁹. Indeed, the murine A β sequence differs from the human one by three amino acids at N-terminal positions 5, 10, and 13 and therefore does not readily aggregate. Curiously, compared to APPKI mice, both APPxPSEN2KO and APPxFADPSEN2 showed an increased plaque deposition in both the cortex and hippocampus from 9 months onwards, with considerable larger plaque area by 18 months of age (Fig. 2a, b, Figure S1f, g). However, clear differences were still observed: plaque pathology was significantly higher in APPxFADPSEN2 at 6 months, while in APPxPSEN2KO, this was only after 9 months. In the cortex, plaque deposition in APPxFADPSEN2 began as early as 3 months. Additionally, APPxPSEN2KO mice showed mainly larger plaques, while APPxFADPSEN2 had more numerous plaques (Fig. 2d, e). Lastly, genotype-specific morphological differences were also apparent. APPKI mice had a common type of plaque consisting of a dense thioflavin-S positive core with a surrounding halo of fibrillar A β positive staining, suggested to act as a reservoir for toxic A β oligomeric species (Fig. 2c)⁵⁰. In contrast, APPxPSEN2KO plaques displayed

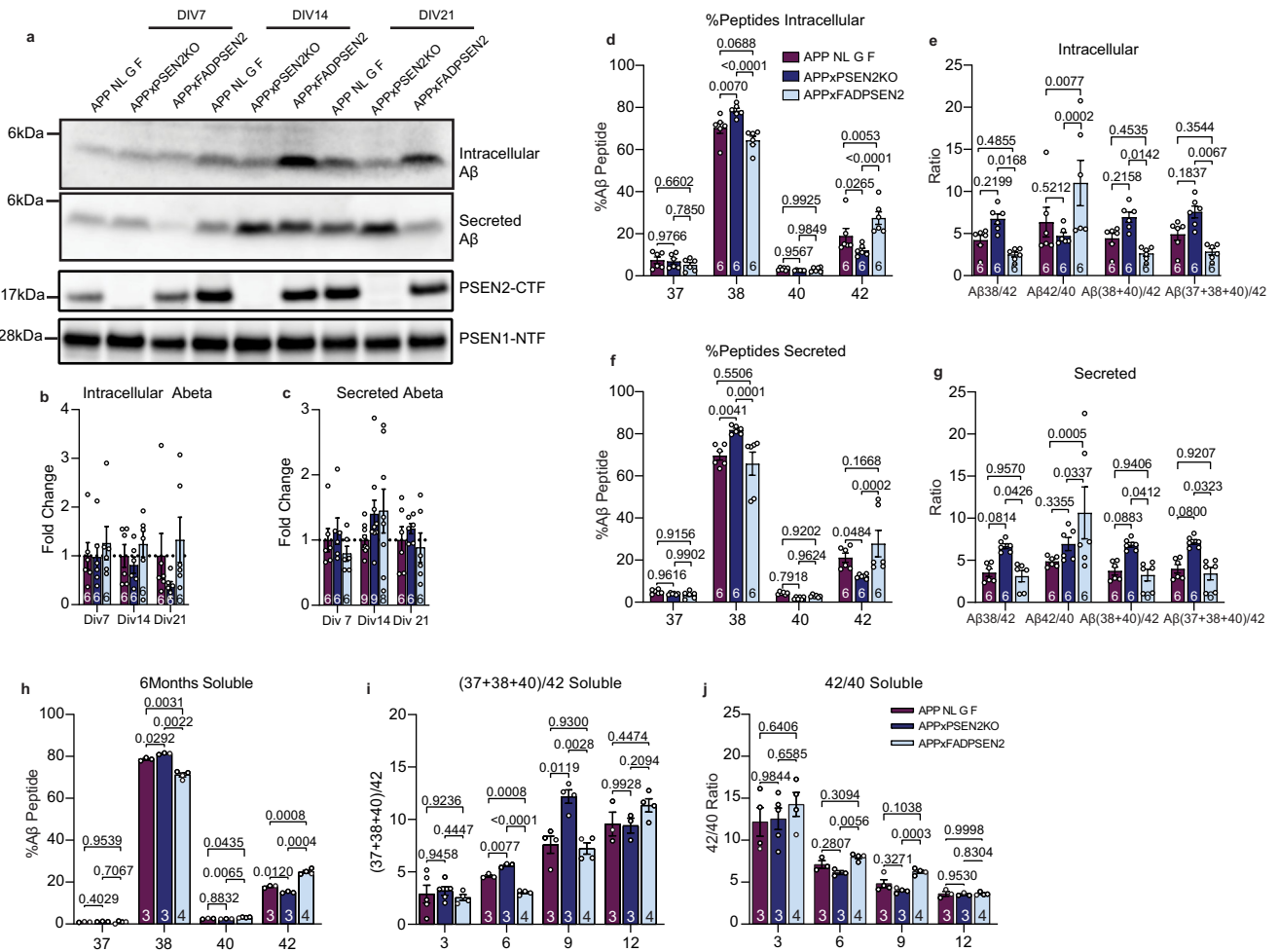


Fig. 1 | Altering PSEN2 expression gives rise to distinct Aβ profiles. **a** Western blot of neuronal lysates collected over time and probed for Aβ, PSEN2-CTF and PSEN1-NTF. **b, c** Quantification of **(a)** for intracellular and secreted Aβ shown as a fold change compared to APPKI. **d–g** MSD ELISA of Aβ species from neuronal lysates (**d, e**) or conditioned medium (**f, g**). **d, f** show the different Aβ peptides compared to total. **e, g** represent Aβ ratios indicating γ-secretase processivity. For

(b–g) samples were collected from 3 different cultures ($N = 3$) where 2 dishes were collected from each culture ($n = 6$). **h–j** MSD ELISA of Aβ species from mouse brain lysate. Statistical analysis was performed using a two-way ANOVA with Tukey’s correction for multiple testing compared to APPKI, p -values and N -numbers are indicated in the figure. All graphs are represented as mean \pm SEM.

a large intensely stained Aβ halo surrounding the dense core, while APPxPSEN2KO presented with a smaller fibrillar Aβ halo largely coinciding with the core, likely linked to Aβ42 shifts from the PSEN2 N141I mutation, and reflecting distinct Aβ profiles and altered aggregation properties between both genotypes compared to APPKI.

Another major hallmark of AD pathology is the accumulation of dystrophic neurites surrounding plaques, identifiable by the accumulation of LAMP1-positive LE/Lys being stalled in neurites around plaques. In both hippocampus and cortex of APPxPSEN2KO mice, LAMP1 immunostaining increased significantly by 3 months compared to APPKI (Fig. 2f, g, Figure S2a–c), preceding plaque pathology (compare with Fig. 2b). APPxPSEN2KO showed no significant LAMP1 increase compared to APPKI mice, except at 9 months in the cortex, at levels similar to APPxPSEN2KO (Figure S2b, c). Transmission EM (TEM) confirmed larger accumulations of degradative compartments in both APPxPSEN2KO and APPxPSEN2KO compared to APPKI (Figure S3). APP-CTFs co-accumulated with LAMP1 in dystrophic neurites across all stages and genotypes, echoing previous studies (Fig. 2f, Figure S2a–d)⁵¹. Overall, both PSEN2KO and FADPSEN2 accelerated plaque pathology in APPKI mice, but impacted plaque morphology and dystrophic neurite accumulation differently, pointing to distinct mechanisms likely driven by altered γ-secretase processivity and iAβ pool compositions.

Altering PSEN2 expression in APP NL G F mice impacts working memory

Since APPxPSEN2KO and APPxPSEN2KO both displayed aggravated AD pathology, we anticipated worsened cognitive deficits. To assess this, we conducted behavioral and memory tests on six month old mice. While circadian rhythm remained unchanged over 24 h, significant differences in activity levels were found (Fig. 3a, b). APPxPSEN2KO mice exhibited hypoactivity compared to both the wild-type and APPKI mice, whereas APPxPSEN2KO mice showed hyperactivity during the night (Fig. 3b). This is in line with previous studies linking hyperactivity in mice with AD pathology⁵².

No differences in locomotion or social memory were observed across genotypes using open field, elevated plus maze and social preference/social novelty (SPSN) tests (Figure S4a–e). However, APPxPSEN2KO mice displayed anxiety, spending less time in open spaces (Figure S4a, b). Therefore, we focused on spatial and working memory, both known to be impaired in AD⁵³. Spatial memory was evaluated using the Morris water maze (Fig. 3c). Considering we observed clear differences in swim speed, time needed to find the platform could not be used as a read out of cognitive function (Figure S4f, g). However, there were no significant differences in distance to the platform during training (Fig. 3d). Moreover, as the time spent in the target quadrant during the probe trial was considerably greater

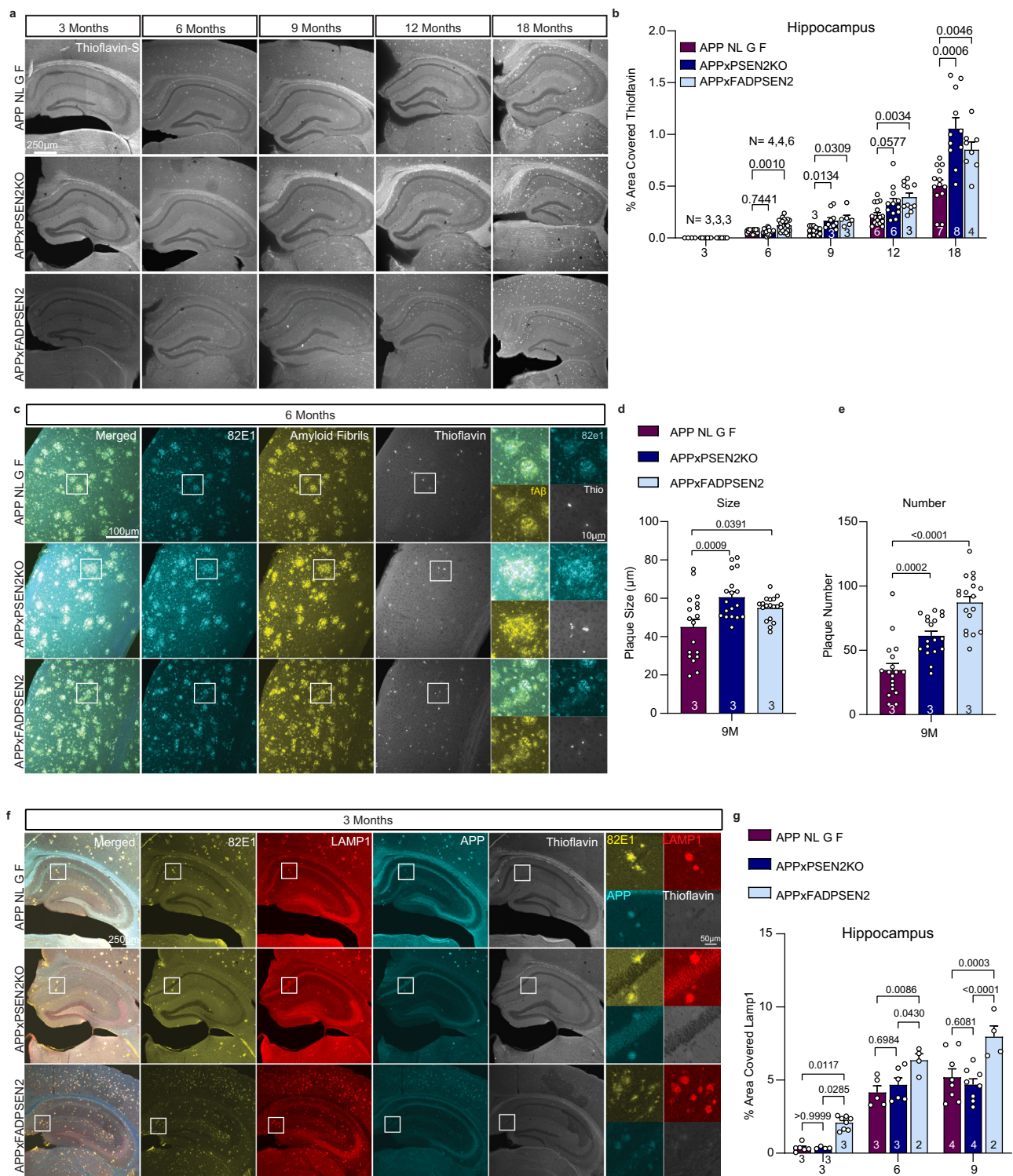


Fig. 2 | PSEN2 deficiency and PSEN2 N141I knock-in both accelerate AD pathology in an APPKI model. **a** Coronal hippocampal slices of APPKI, APPxPSEN2KO and APPxFADPSEN2 stained for thioflavin, labelling dense core plaques over time. **b** Quantification of thioflavin⁺ area normalized to brain area for hippocampus over time and analyzed using two-way ANOVA using a Dunnett's correction for multiple testing comparing the different conditions to APPKI. **c** Dual immunolabelling of A β plaques in coronal cortex sections using a fibrillar (fA β) and monomeric A β specific antibody (82e1). **d, e** Average size (**d**) and number (**e**) of thioflavin⁺ plaques calculated from (**a, c**). Statistical analysis was through a one-way

ANOVA with a Dunnett's correction for multiple testing compared to APPKI (**f**). Immunolabelling of 3 month old coronal hippocampal slices of APPKI, APPxPSEN2KO and APPxFADPSEN2 for A β /APP-CTF (82e1), LAMP1, full length APP and thioflavin. **g** Quantification of LAMP1⁺ area as a percent of total hippocampus area. For (**g**) a two-way ANOVA analysis with Tukey's correction for multiple testing compared to APPKI was used. Scale bars and *p*-values are indicated; number of mice (N) is shown inside the bar and the symbols represent the number of regions analyzed. All graphs are mean \pm SEM.

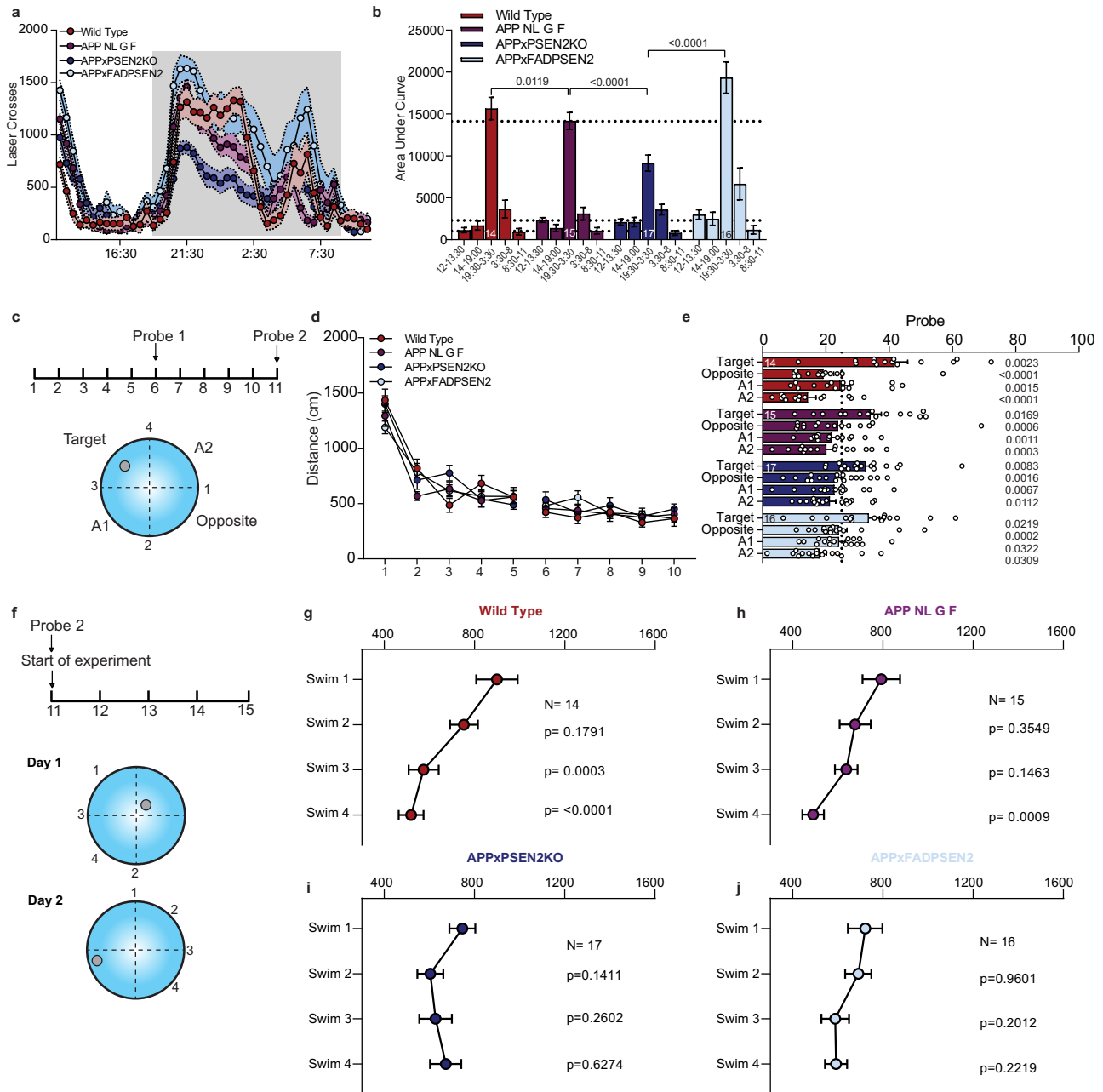


Fig. 3 | PSEN2 deficiency and FAD-linked mutant PSEN2 lead to working memory deficits. For all the behavioral tests the cohorts consist of wild-type $N = 14$, APP NL G F $N = 15$, APPxPSEN2KO $N = 17$, APPxFADPSEN2 $N = 16$ where N represents individual female mice. **a** Total laser crossings of wild-type, APPKI, APPxPSEN2KO and APPxFADPSEN2 mice summed per 30 min and represented over time. Gray square indicates nocturnal hours with increased activity. **b** Area under the curve calculated based on graph represented in A. Statistical analysis was done using one-way ANOVA with Dunnett's correction for multiple testing comparing to APPKI. **c** Schematic of the Morris water maze paradigm with 10 training days and a probe trial on day 6 and day 11. **d** Average distance swam to find the platform per

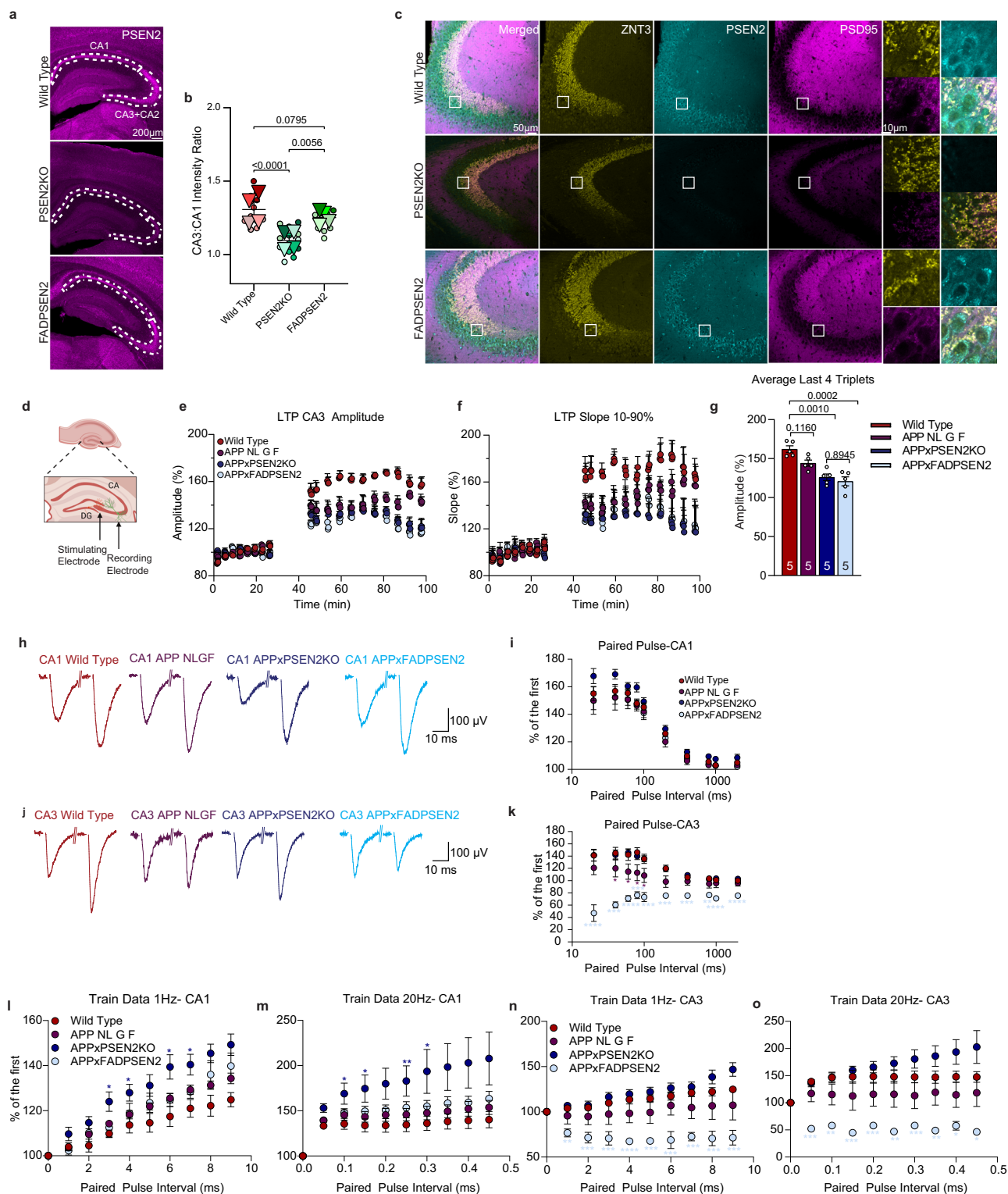
genotype per day over the total training period. **e** Average time spent in the target quadrant versus other quadrants. For time spent in target quadrant, a two-tailed t-test was used comparing average to 25% indicating presence in quadrant is higher than chance level. For comparison of time spent in other quadrants versus target, one-way ANOVA was performed with Dunnett's multiple comparisons test. **f** Schematic of the matching to platform paradigm with 5 total testing days. **g–j** Average distance swam over the different daily trials averaged over the total testing days. Subsequent swims were compared to swim 1 using a one-way ANOVA with Tukey's corrections for multiple testing. All graphs are mean \pm SEM, with p - and n -values indicated.

than chance for all genotypes, we concluded that both learning and spatial memory are not significantly different between genotypes (Fig. 3e). Working memory was tested using the delayed matching to platform (DMTP), a variant of the Morris water maze where platform location changed daily (Fig. 3f). APPKI mice showed a significant decrease only by the final swim, underscoring early deficits in working memory compared to wild-type mice (Fig. 3g, h). Neither APPxPSEN2KO nor APPxFADPSEN2 mice were able to reduce their swimming

distances throughout trials, indicating an earlier and more severe working memory impairment compared to wild-type and APPKI mice (Fig. 3i, j).

Working memory deficits correlate with defects in mossy fiber-CA3 hippocampal circuitry

Given the distinct amyloid pathology in the hippocampus of APPxPSEN2KO vs APPxFADPSEN2 mice (Fig. 2a, b) and PSEN2-related



working memory deficits, we wondered whether this could stem from brain region-specific PSEN2 expression differences. Since PSEN2 also accumulated in LE/Lys in dystrophic neurites around plaques in our AD models, we first examined its localization in wild-type mice (Figure S5a). Notably, endogenous PSEN2 was more highly expressed in the CA3 and subiculum regions of the hippocampus (Fig. 4a, Figure S5b). Quantitative comparison of the CA3 and CA1 areas confirmed the higher PSEN2 levels in the CA3 (Fig. 4b). This was recapitulated in FADPSEN2, with overall higher expression in the cortex, as noticed by

western blotting (Figure S1d). Co-staining with a mossy fiber-specific marker, zinc transporter 3 (ZNT3), revealed PSEN2-positive cells near mossy fiber synapses within the CA3 region in wild-type and mutant PSEN2 mice (Fig. 4c) The hippocampus receives input through the entorhinal cortex, signaling to the dentate gyrus, and then via mossy fibers (MFs) to CA3 pyramidal neurons, which play a role in working memory³⁴. As PSEN2 is highly expressed in CA3 pyramidal cells, we investigated long-term potentiation (LTP) in APPxPSEN2KO and APPxFADPSEN2 mice (Fig. 4d). Consistent with previous reports, using

Fig. 4 | CA3 localized PSEN2 is required for hippocampal circuitry and LTP.

a Representative confocal images of PSEN2 immunoreactivity in coronal sections of hippocampus from wild-type, PSEN2KO and FADPSEN2 mice; quantified in **(b)** as a CA3/CA1 ratio. Wild type, N(number of mice)=4, n(total slices analyzed)=12, PSEN2KO $N = 4$ $n = 12$, FADPSEN2 $N = 4$, $n = 7$. Statistical analysis was performed using one-way ANOVA with Dunnett's correction for multiple testing compared to wild type. **c** Representative images from the hippocampal CA3 region of wild-type, PSEN2KO and FADPSEN2 mice immunostained for PSEN2, ZNT3 and PSD95. Representative images were selected from 3 different mice stained per genotype. **d** Schematic of the recording and stimulating electrodes. Created in BioRender. Vranx, C. (2024) <https://BioRender.com/j96p125>. **e** fEPSPs recorded from mossy fiber-CA3 synapses in 6 month old wild-type, APPKI, APPxPSEN2KO and APPx-FADPSEN2 mice. After 30 min of baseline recordings, LTP was induced by two trains of 75hz stimulation and fEPSPs recorded for 50 min. **e** LTP amplitude. **f** LTP slope. For both amplitude and slope wild type $N = 5$, APPNLGF $N = 5$, APPxPSEN2KO $N = 5$, APPx-FADPSEN2 $N = 5$ where N represents individual mice. **g** Average amplitude for the last four triplicate fEPSPs compared to wild-type. Statistical analysis was done using a one-way ANOVA with Dunnett's test for multiple comparisons. **h** Representative traces from paired pulse recordings in CA1 plotted with 40 ms interval. Double line is used to indicate additional time passing. **i** Paired pulse results from the CA1 region represented as %amplitude from the first recorded amplitude. Number of mice (N) and cells (n) recorded: Wild type $N = 5$ $n = 10$, APPKI $N = 5$ $n = 9$, APPxPSEN2KO $N = 5$ $n = 10$, APPx-FADPSEN2 $N = 5$ $n = 9$. **j** Representative traces from paired pulse recordings in CA3 plotted with 40 ms interval. Double line is used to indicate additional time passing. **k** Paired pulse results from the CA3

region represented as %amplitude. Statistical analysis was performed per interval using a one-way ANOVA with Dunnett's correction for multiple testing comparing genotypes to wild type. Exact p -values: 20 ms***= <0.0001 , 40 ms***= 0.0003 , 60 ms*= 0.0338 , ****= <0.0001 , 80 ms*= 0.0204 , ***= 0.0001 , 100 ms*= 0.0380 , ***= 0.0003 , 200 ms*= 0.0285 , ***= 0.0006 , 400 ms***= 0.0003 , 800 ms**= 0.0011 , 1000 ms***= <0.0001 , 2000ms***= <0.0001 . Number of mice (N) and cells (n) recorded: Wild type $N = 3$ $n = 5$, APPKI $N = 4$ $n = 5$, APPxPSEN2KO $N = 5$ $n = 7$, APPx-FADPSEN2 $N = 3$ $n = 4$. **l-o** Train stimulation data for the CA1 and CA3 respectively with each graph representing a different stimulus strength. Response is calculated as % of the total first response with increasing paired pulse interval. Statistical analysis was performed per interval using a one-way ANOVA with Dunnett's correction for multiple testing, always comparing to wild type. Exact p -values CA1 1 Hz 3 ms*= 0.0256 , 4 ms*= 0.0430 , 6 ms*= 0.0282 , 7 ms*= 0.0484 . CA1 20 Hz 0.1 ms*= 0.0117 , 0.15 ms*= 0.0137 , 0.25 ms**= 0.0087 , 0.3 ms*= 0.0218 . CA3 1 Hz 1 ms**= 0.0015 , 2 ms***= 0.0006 , 3 ms***= 0.0007 , 4 ms***= <0.0001 , 5 ms***= 0.0001 , 6 ms***= 0.0001 , 7 ms***= 0.0001 , 8 ms***= 0.0007 , 9 ms***= 0.0008 . CA3 20 Hz 0.05 ms***= 0.0007 , 0.1 ms**= 0.0022 , 0.15 ms***= 0.0008 , 0.2***= 0.0005 , 0.25**= 0.0039 , 0.3 ms***= 0.0007 , 0.35 ms**= 0.0012 , 0.4 ms*= 0.0297 , 0.45*= 0.0432 . Number of mice (N) and cells (n) recorded for CA1: Wild-type $N = 5$ $n = 10$, APPKI $N = 5$ $n = 9$, APPxPSEN2KO $N = 5$ $n = 10$, APPx-FADPSEN2 $N = 5$ $n = 9$. Number of mice (N) and cells (n) recorded for CA3: Wild-type $N = 5$ $n = 9$, APPKI $N = 4$ $n = 5$, APPxPSEN2KO $N = 5$ $n = 7$, APPx-FADPSEN2 $N = 3$ $n = 4$. All graphs are represented as mean \pm SEM and include p -values.

a mild LTP induction procedure, APPKI mice displayed a modest reduction in LTP amplitude and slope⁵². Interestingly, LTP was further reduced in acute brain slices of both APPxPSEN2KO and APPx-FADPSEN2 mice (Fig. 4e–g) in line with observed working memory deficits (Fig. 3i, j), and tying PSEN2 expression to hippocampal circuitry and signaling. Specifically, the data suggest a defect in late phase LTP, implying issues in local and/or somatic de novo protein replenishment^{55,56}. Additionally, the amplitude distribution of input-output (IO) curves were consistently larger in APPxPSEN2KO and APPx-FADPSEN2 compared to control and APPKI mice (Figure S5c, d), indicating potential differences in synaptic composition/function.

To exclude a global hippocampal deficit, we measured LTP in the CA1 region and found no significant differences between genotypes (Figure S5e–g). We then explored short-term presynaptic plasticity using paired-pulse stimulations in the CA1 and CA3 regions. APPxPSEN2KO mice showed increased synaptic facilitation in the CA1, while in the CA3, PSEN2KO rescued the lowered response seen in APPKI to wild-type levels. In contrast, APPx-FADPSEN2 mice displayed clear synaptic depression in the CA3 circuit, with normal responses in CA1 (Fig. 4h–k). To investigate the effects on presynaptic dynamics during periods of more demanding synaptic activity, we performed train stimulations in both hippocampal regions. In line with the paired pulse data, we observed increased synaptic facilitation in the APPxPSEN2KO predominantly in CA1 and partially in CA3, while APPx-FADPSEN2 mice showed clear synaptic depression, exclusively in the CA3 circuit (Fig. 4l–o, Figure S5h). Taken together, these results indicate alterations to synaptic efficacy in both the APPxPSEN2KO and APPx-FADPSEN2 mice, likely involving presynaptic changes in the organization of the synaptic vesicle pool (see below). In case of the APPx-FADPSEN2 this is more specific to the CA3 region whereas for the APPxPSEN2KO this is observed in both CA3 and CA1 but without impacting LTP in the CA1.

We next used TEM to investigate morphological changes in the MF-CA3 circuit. These structurally distinct synapses consist of a large presynaptic axons synapsing onto multiple CA3 pyramidal neurons⁵⁷. They can be easily distinguished ultrastructurally through the presence of large, dense clusters of synaptic vesicles, as seen in wild-type CA3 regions (Fig. 5a, Figure S5i). While there was a moderate, non-significant decrease in synapse area in APPKI CA3 regions, significant decreases were noticed in APPxPSEN2KO and APPx-FADPSEN2 mice

(Fig. 5b). Post-synaptic densities (PSDs) were also significantly reduced in number and length across AD genotypes, compared to wild-type (Fig. 5c–d), with APPx-FADPSEN2 having the largest decrease in PSD number (Fig. 5c) and APPxPSEN2KO the largest decrease in PSD length per synapse (Fig. 5d). At higher resolution, synaptic vesicle clusters displayed distinct morphological features (Fig. 5f, Figure S5i). They did not differ between wild-type and APPKI, but synaptic vesicle cluster density was significantly higher in APPxPSEN2KO while lower or more sparse in APPx-FADPSEN2 synapses (Fig. 5e); correlating with electrophysiological and LTP differences (Fig. 4). Additionally, both APPxPSEN2KO and APPx-FADPSEN2 synapses showed higher heterogeneity in vesicle size through the presence of larger vesicles (white arrowheads, in Fig. 5f, Figure S5i). Overall, these results highlight both pre- and post-synaptic changes linked to altered PSEN2 expression in MF-CA3 synapses. To investigate underlying molecular mechanisms, we turned to primary hippocampal neurons derived from E17 APPKI, APPxPSEN2KO and APPx-FADPSEN2 embryos.

PSEN2-related synaptic defects are recapitulated in primary hippocampal neurons

First, we aimed to determine if PSEN2/ γ -secretase complexes are in close proximity of synapses. Super-resolution imaging revealed small PSEN2-positive LE/Lys (marked by LAMP1) near the post-synaptic marker, PSD95, in APPKI and APPx-FADPSEN2 neurons (Fig. 6a, white arrowheads). Quantification showed no significant difference in the overlap of PSD95 with PSEN2 positive LE/Lys (Fig. 6c), indicating that the FAD mutation did not affect their postsynaptic abundance. Compared to wild-type, APPKI exhibited a significant decrease in both number and size of PSD95-positive post-synapses, which was recapitulated in APPxPSEN2KO (Fig. 6d, e, Figure S6d). In APPx-FADPSEN2, only size of post-synapses was significantly decreased. Even though PSEN2 is mainly in dendrites, it was also found on LAMP1-positive vesicles in axons and near synaptobrevin2-positive pre-synapses, highlighting the presence of PSEN2 in both pre- and post-synaptic compartments (Fig. 6b, f, Figure S6a, 6c).

Synaptic plasticity relies on coordinated synaptic signaling through pre-synaptic neurotransmitters binding to post-synaptic receptors. Two essential proteins are the presynaptic vGLUT1, a glutamate transporter involved in synaptic vesicle refilling, and the postsynaptic GLUA1, a subunit of the AMPA receptor complex crucial

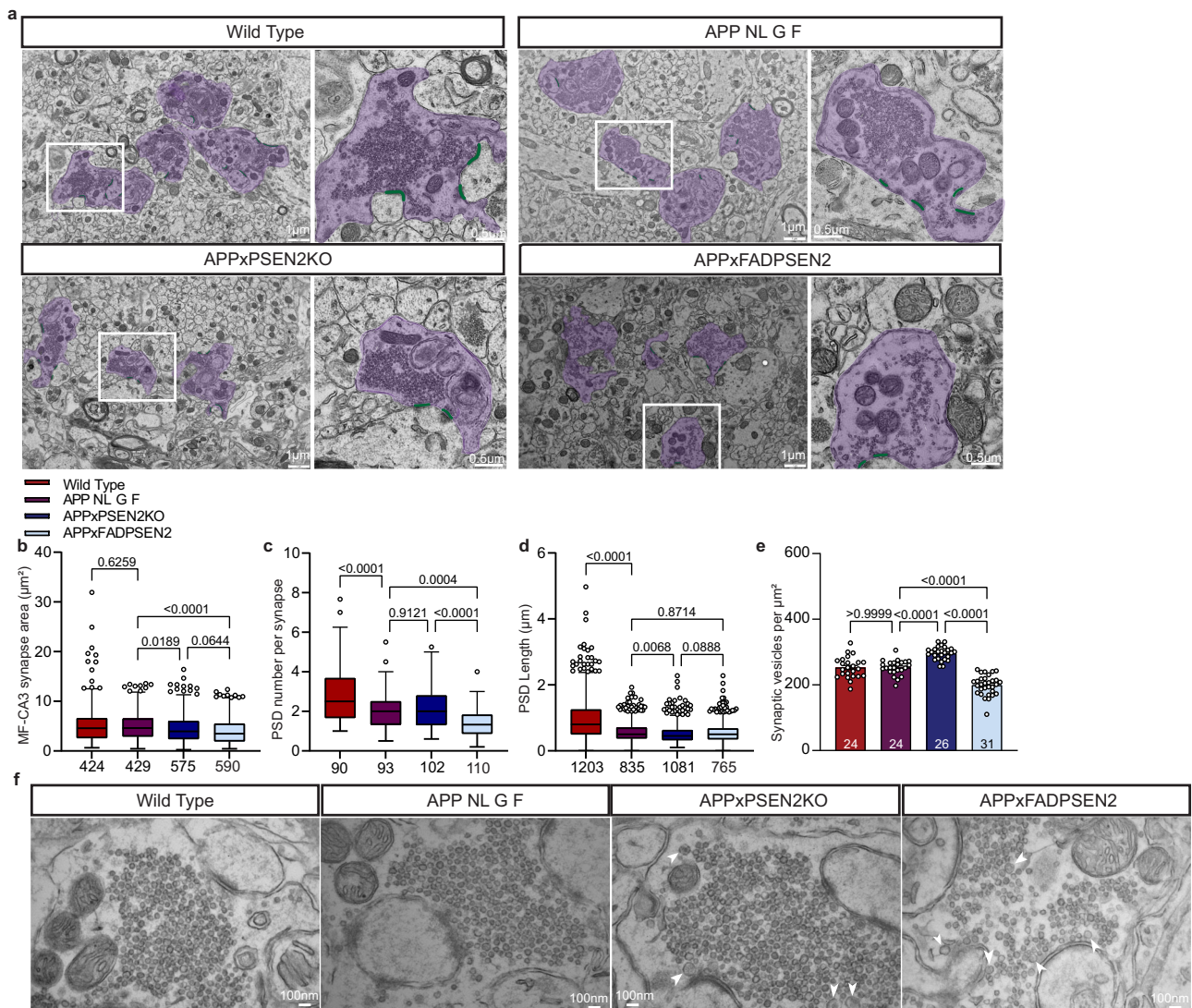


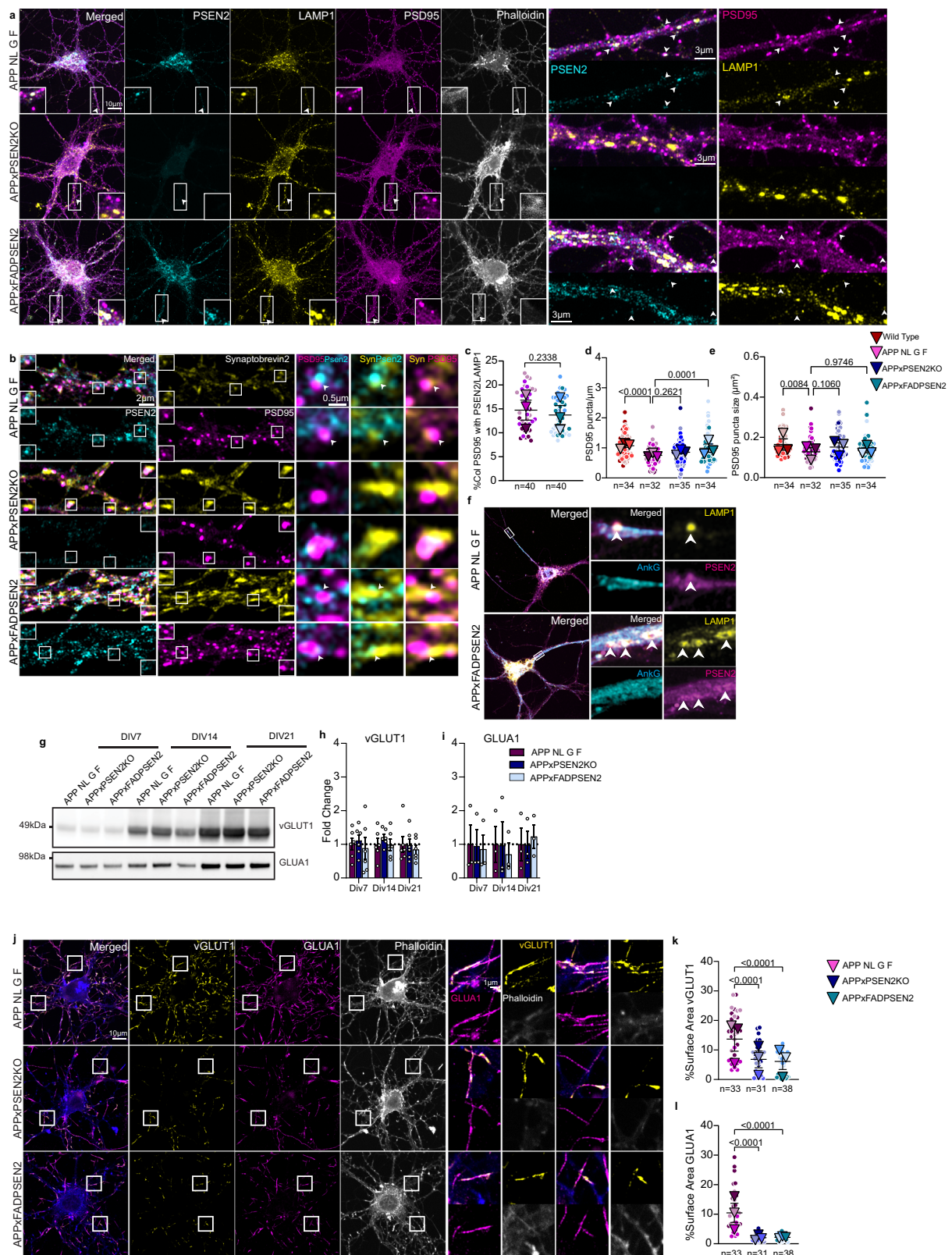
Fig. 5 | Altering PSEN2 expression affects ultrastructural morphology of mossy fiber synapses. **a** Representative TEM images of mossy-fiber CA3 synapses in coronal sections of 6-month-old wild type, APPKI, APPxPSEN2KO and APPxFADPSEN2 mice. The purple area highlights synapse area, the green postsynaptic densities. Representative images were selected from 3 different mice analyzed per genotype. **b** Mossy fiber-CA3 pre-synaptic area as measured from images shown in (a). **c** Average postsynaptic density number per synapse. **d** Average postsynaptic density length in μm . Data in b-d are represented using Tukey box and whisker

plots. **e** Synaptic vesicles density per μm^2 as quantified from images as shown in (f). **f** Representative TEM images of presynaptic vesicle clusters. Number beneath the graphs or in bars represent number of synapses, number of vesicles or number of postsynaptic densities calculated from an $N=3$ mice. White arrow heads indicate enlarged vesicles. For (b–e) Statistical analysis was done using one-way ANOVA with Dunnett's correction for multiple testing, each genotype compared to another. All graphs are represented as mean \pm SEM and scale bars are represented in images.

for LTP⁵⁸. We observed no significant differences in the total levels of either receptor, or in the phosphorylation state of GLUA1 (Fig. 6g–i, Figure S6b). However, surface levels of vGLUT1 and GLUA1 were significantly decreased in APPxPSEN2KO and APPxFADPSEN2 neurons compared to APPKI (Fig. 6j–l, Figure S6e). Considering total levels remained unchanged (Fig. 6g), this suggests a PSEN2-dependent recycling defect, potentially causing the observed synapse morphology and LTP defects, and contributing to working memory impairments in these PSEN2 AD mouse models. Given that PSEN2/ γ -secretase is largely restricted to LE/Lys²⁹, and present both pre- and post-synaptically, we hypothesize that LE/Lys dysregulation may underpin these synaptic alterations.

Altered PSEN2 expression causes lysosomal defects in neurons
Synapses are highly active compartments relying heavily on the endolysosomal system for proper degradation, recycling and trafficking of synaptic receptors⁵⁹. Previous studies indicated that A β 42

preferentially concentrated in LE/Lys compartments^{60–62} affecting their integrity. Also aberrant levels of the γ -secretase substrate, APP β -CTF, cause endosomal to lysosomal dysfunctions, observed for APP and PSEN1 mutations^{63,64}, and in Down Syndrome⁶⁵. To explore APP fragment accumulation in LE/Lys of our PSEN2 AD models, we performed co-immunostaining with 82e1, recognizing both APP β -CTF and A β , and Y188 antibodies, which targets full-length APP and APP-CTFs. Organelles positive for both antibodies identify APP β -CTF buildup, whereas 82e1-only organelles point to A β accumulation. Significantly more 82e1/Y188-positive LE/Lys were found in hippocampal neurons of APPxPSEN2KO and APPxFADPSEN2 mice, compared to APPKI, denoting APP fragment accumulation (Fig. 7a–d). As expected, absence of PSEN2 expression resulted in more frequent co-apposition of 82e1 and Y188, underscoring APP- β CTF buildup in LAMP1-positive LE/Lys (Fig. 7a, white arrowheads). Conversely, APPxFADPSEN2 neurons showed more intense 82e1 immunostaining, with 82e1-only immunoreactivity more common in LAMP1-positive LE/Lys, confirming



increased Aβ levels (Fig. 7a, orange arrowheads). There was also significantly more overlap between LAMP1-positive LE/Lys and Y188/82e1 in APPxPSEN2KO and APPxFADPSEN2, solidifying accumulation of APP fragments (Fig. 7c). Finally, western blot analysis also revealed higher APP-CTFs levels in APPxPSEN2KO and APPxFADPSEN2 neurons (Fig. 7b, d). Of note, immunostaining for APP fragments was not restricted to LE/Lys indicating accumulation in other endosomal

compartments. In summary, both APPxPSEN2KO and APPxFADPSEN2 neurons presented significant and distinct accumulation of APP fragments that may disrupt endolysosomal homeostasis, as reported in other models (see above).

Not surprisingly, given the preferred location of PSEN2 in LE/Lys, APPxPSEN2KO and APPxFADPSEN2 hippocampal neurons presented with significantly increased LAMP1-positive organelles compared to

Fig. 6 | PSEN2 expression in LE/Lys is required to maintain pre- and post-synaptic homeostasis. **a** Representative images of DIV14 hippocampal neurons immunostained for PSEN2, LAMP1, PSD95 and Phalloidin. Zoomed insets show PSEN2 within LAMP1⁺ compartments close to PSD95 spots (highlighted by white arrow heads). **b** Representative images of PSEN2 in close proximity to post synaptic (PSD95) and presynaptic (Synaptobrevin2) compartments, further highlighted in zoomed insets (white arrow heads). **c** Quantification of %overlap of PSD95 with PSEN2 and LAMP1⁺ puncta in APPKI and APPx^{FAD}PSEN2 neurons from images in (a). **d, e** Quantification of PSD95 puncta per μm (**d**) and size (**e**) from images in (a, b). **f** Representative images of DIV14 hippocampal neurons immunostained for PSEN2,

LAMP1 and AnkyrinG, a marker of the axonal initial segment. Zoomed insets highlight PSEN2⁺/LAMP1⁺ vesicles in axons. Representative images were selected from two different coverslips stained from one culture. **g** Representative western blot of neuronal lysates probed for vGLUT1 and GLUA1 and quantified in (h) (vGLUT1) and (i) (GLUA1). **j** Representative images of DIV 14 hippocampal neurons immunostained for surface vGLUT1 and GLUA1, and with Phalloidin to label F-actin; quantified in (k) (vGLUT1) and (l) (GLUA1). All statistics were done by one-way ANOVA with Tukey's correction for multiple testing compared to APPKI. All graphs are mean \pm SEM and indicate scale bars and *p*-values. Triangles and circles represent the average per neuronal culture and individual cells, respectively.

APPKI neurons (Fig. 7e, f). There was a moderate increase in early endosomal compartments (Fig. 7g, EEA1⁺), with no differences in recycling endosomes (Fig. 7h, VPS35⁺). More frequent overlap of all three markers in APPx^{PSEN2KO} and APPx^{FAD}PSEN2 neurons (Fig. 7e, white arrowheads), suggested partial endolysosomal collapse. To investigate lysosomal dysfunction, we assessed Ca²⁺ storage, crucial for lysosomal fusion and fission⁶⁶. Treatment with the TRPML1 agonist, MLSA1⁶⁷, resulted in a significantly lower Ca²⁺ release from LE/Lys of APPx^{PSEN2KO} and APPx^{FAD}PSEN2 neurons (Figure S6f, g). To corroborate this, we allowed neurons to endocytose dextran-488 and the Ca²⁺ sensitive rhodamine-dextran, that, when chased to LE/Lys allowed us to directly visualize basal lysosomal Ca²⁺ levels. In APPx^{PSEN2KO} and APPx^{FAD}PSEN2 neurons, rhodamine intensity in dextran-488-positive vesicles is clearly decreased, confirming lowered lysosomal Ca²⁺ content compared to APPKI neurons (Fig. 7i, j). This was coupled to a substantial decrease in lysosomal exocytosis, as shown by surface localized LAMP1 immunostaining (Fig. 7k, l). Next, neurons were transfected with the dual labelled LC3 allowing to distinguish autophagosomes from autolysosomes (Fig. 7m). Both organelles were more abundant in APPx^{PSEN2KO} and APPx^{FAD}PSEN2 neurons, demonstrating an imbalanced autophagy, and including a congestion in the degradative capacity, evidenced by the significant increase in autolysosomes (Fig. 7m–p). These findings link the aberrant accumulation of APP metabolic fragments, due to either PSEN2KO or FADPSEN2, to impaired LE/Lys and autophagic functions, which could in turn affect synaptic receptor recycling/trafficking underlying the observed synaptic defects.

Discussion

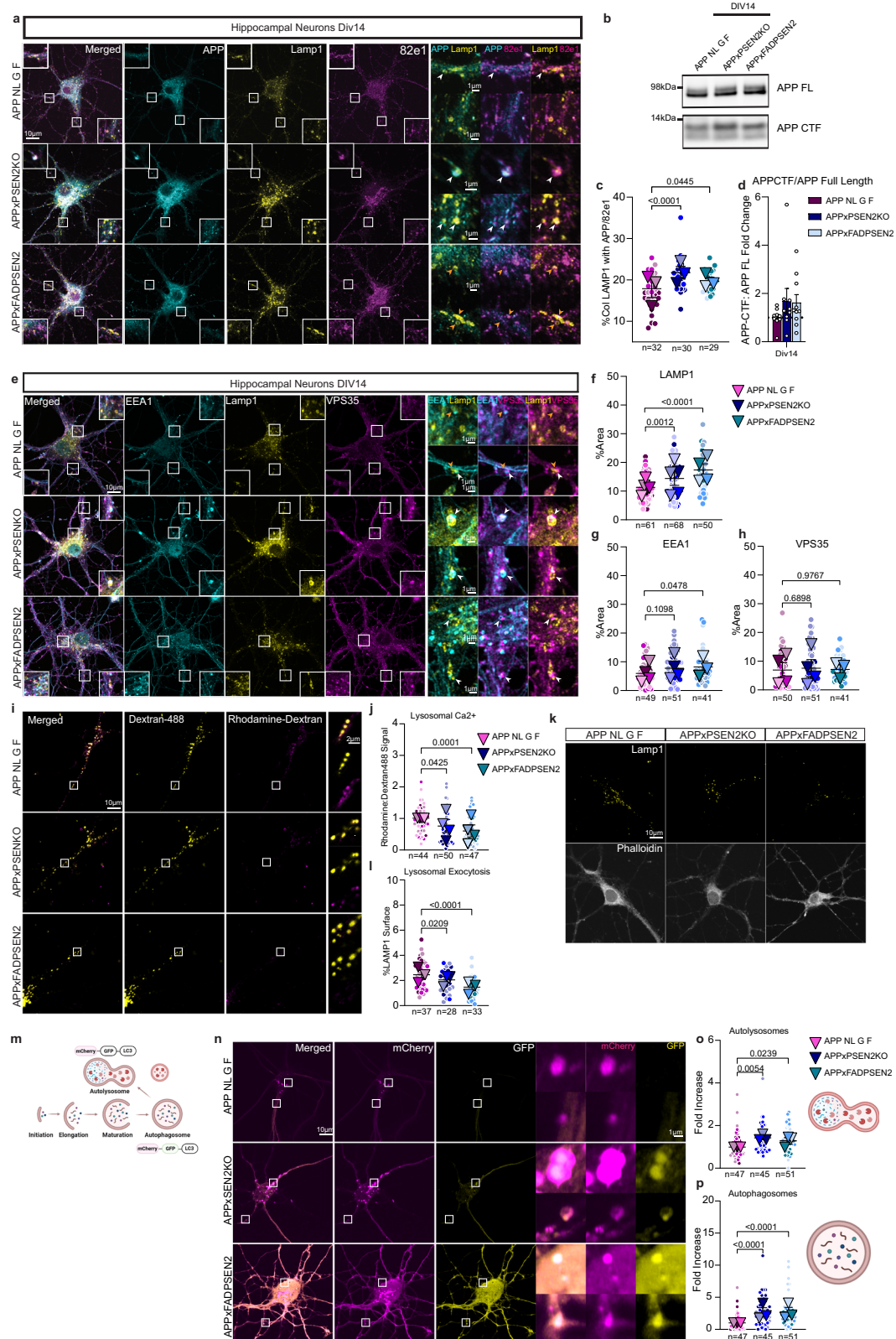
γ -Secretases have been central to AD pathology for decades. However, understanding the impact of full γ -secretase inactivity, either pharmacologically⁶⁸ or genetically⁶⁹, on cell functioning does not reflect disease conditions. How altered function of individual complexes contributes to disease remains unknown and filling in this knowledge gap is key to understand disease progression. Here, we studied how PSEN2 deficiency versus a FAD-associated PSEN2 N141I KI mutation impacts AD pathogenesis in APPKI mouse models. Importantly, the use of an APPKI mouse model was necessary to address this question since, as previously mentioned, wild-type mice do not develop A β pathology⁴⁹. Despite distinct A β profiles, both PSEN2 genotypes accelerated AD pathology, evidenced by earlier plaque deposition, more dystrophic neurites and more severe memory deficits (Fig. 8). These defects correlated with increased PSEN2 expression in the hippocampal CA3, lower LTP in the mossy fiber circuit and ultrastructural changes such as smaller presynaptic boutons, shorter or fewer PSDs and altered synaptic vesicle pools. Supporting in vivo data, primary hippocampal neurons from these models showed decreased surface expression of presynaptic vGLUT1 and postsynaptic GLUA1 in APPx^{PSEN2KO} and APPx^{FAD}PSEN2 mice. We hypothesize that endolysosomal dysregulation underlies these synaptic alterations. Knocking-out or mutating PSEN2 leads to aberrant accumulation of APP metabolic products in LE/Lys, affecting lysosomal homeostasis (e.g., reduced lysosomal Ca²⁺) resulting in decreased lysosomal exocytosis and a degradative bottleneck indicated by accumulating LC3-

positive autophagosomes and autolysosomes. Our data underscore that PSEN2/ γ -secretase maintains LE/Lys homeostasis, essential for synaptic integrity, especially in areas with higher PSEN2 expression, like the CA3.

The accelerated amyloid pathology in APPx^{FAD}PSEN2 brains correlated with decreased γ -secretase processivity and a toxic gain-of-function by producing more A β 42⁷⁰. Not surprisingly, compared to APPKI, we observed denser thioflavin⁺ plaques, composed mostly of A β 42 with a filamentous A β halo⁷¹. This compacted halo contrasted with the larger, diffuse plaques in APPx^{PSEN2KO} brain, which correlated with increased processivity and shorter, less aggregation-prone A β peptides. The absence of PSEN2 directs APP metabolism toward PSEN1/ γ -secretase, at the cell surface and in early/recycling endosomes. Thus, these diffuse plaques likely originate from secreted relatively shorter A β , as increased A β secretion was observed in APPx^{PSEN2KO} primary neurons (Fig. 1). In contrast, APPx^{FAD}PSEN2 brains and hippocampal neurons showed decrease secreted A β , compensated by intracellular A β 42 accumulation, consistent with observations in transgenic overexpression models^{72,73}. This provides in vivo support for PSEN2/ γ -secretase as the main generator of iA β , which significantly increases in FAD settings, whilst PSEN1 preferentially contributes more to secreted A β ²⁹. Secondly, the APPx^{PSEN2KO} data confirm that PSEN2 inherently favors the production of longer A β peptides whereas PSEN1 complexes produce shorter ones, in line with human iPSC studies⁷⁴.

The arctic mutation in the APPKI model enhances protofibril generation of A β 40 peptides⁷⁵, meaning fibrils in this model may not fully represent human pathology⁷⁶. Therefore, the observed alterations in amyloid pathology may be in part due to the presence of this mutation. However, distinct plaque types, from diffuse to fibrillar and dense core, are also observed in human brains^{77,78}; including in sporadic and certain FAD cases^{79,80}. As plaque fibrils result from A β self-assembly which is dependent on peptide length and other modifications⁷⁸, altering γ -secretase processivity profiles, as seen in our PSEN2 mutant lines, may indeed lead to altered plaque morphologies in a physiologically more relevant AD context.

Noting the clear exacerbation of pathology, we behaviorally analyzed these mouse models. Behavioral studies of the APP NLGF model have produced conflicting results, with some reporting memory impairments at 6 months whilst others did not^{48,81–83}. In our paradigms, spatial, social and learning memory appeared unaffected for all models, including APP NLGF, compared to wild-type. However, altering PSEN2 levels in this APPKI background clearly led to specific behavioral changes. When observed for 24h, APPx^{PSEN2KO} mice appeared hypoactive without disrupted circadian rhythm, whilst APPx^{FAD}PSEN2 mice exhibited hyperactivity. Hyperactivity in mice suggests hyperactive neural circuits⁸⁴, an early sign in disease progression due to altered functional connectivity^{85,86}. This hyperactivity has been shown in several FADPSEN2 transgenic models, particularly in the hippocampus^{87–90} and increasing susceptibility to seizures⁸⁶, a symptom also observed in AD patients with PSEN2 FAD mutations. In contrast, PSEN2KO mice are more resistant to seizure kindling, especially at younger ages^{91,92}. Much of the FAD-linked hyperexcitability has been attributed to toxic A β species, either through direct binding to



synaptic receptors⁹³, reducing inhibitory synapses^{94,95} or modulating excitatory signaling^{96–98}.

We observed a specific working memory deficit linked to PSEN2 deficiency or FAD-linked KI mutation, compared to only slight impairments in the APPKI mice. Working memory is closely associated with CA3 and resident mossy fiber-pyramidal cell synapses, which are impaired early in AD^{99–101}. Our data also show higher expression of

PSEN2 within CA3 circuits, implicating it in working memory (Fig. 4). Altering PSEN2 expression reduced LTP in the mossy fiber circuit, compared to wild-type mice, indicating significant changes in synaptic function in APPxPSEN2KO and APPxPSEN2 models. At the ultrastructural level, synaptic vesicle clusters were more dense in APPxPSEN2KO and less dense in APPxPSEN2 mossy fiber synapses, highlighting the need for normal PSEN2 expression to maintain

Fig. 7 | Endolysosomal imbalance in hippocampal neurons deficient for PSEN2 or expressing the PSEN2 N141I mutant. **a** Representative images of DIV14 hippocampal neurons immunostained for full length APP, APPCTF/Ab β (82e1) and LAMP1. Arrowheads in zoomed insets highlight co-localization. **b** Western blot of DIV14 neuronal lysates showing increased APP-CTF levels. **c** Quantification of a for triple overlap between LAMP1 and APP/82e1 positive puncta. **d** Quantification of ratio APP: APP-CTF ratio of blots from (b). **e** Representative images of immunolabeling of early (EEA1) and recycling endosomes (VPS35), and LE/Lys (LAMP1). White arrowheads in zoomed insets show overlap between three compartments. **f-h** Quantification of total area of (f) LAMP1, (g) EEA1 and (h) VPS35 as percentage of total neuronal soma area. **i** Representative images of lysosomal Ca $^{2+}$ measured through feeding cells with dextran coupled Alexa488 and Ca $^{2+}$ sensitive Rhodamine-coupled dextran, and quantified in (j) as a Rhodamine/Alexa488 ratio.

k LAMP1 surface labelling combined with Phalloidin staining, quantified in (l). **m** Schematic of the dual labelled mCherry-GFP-LC3: in autophagosomes both mCherry and GFP give yellow fluorescence; whereas in lysosomes, GFP is quenched resulting in red fluorescence. Created in BioRender. Vrancx, C. (2024) <https://BioRender.com/j26q595>. **n** Representative images of DIV14 hippocampal neurons transfected with mCherry-GFP-LC3, quantified in (o) as total number of mCherry+ LC3 puncta normalized to APPKI neurons and in (p) as total number of mCherry + / GFP + LC3 puncta. Graphs (c-f-g-h-j-l-o-p) were statistically analyzed using one-way ANOVA with Tukey's correction for multiple testing compared to APPKI. All graphs are represented as mean \pm SEM, with triangles and circles representing the average per neuronal culture and individual cells, respectively. Scale bars are indicated in the figure.

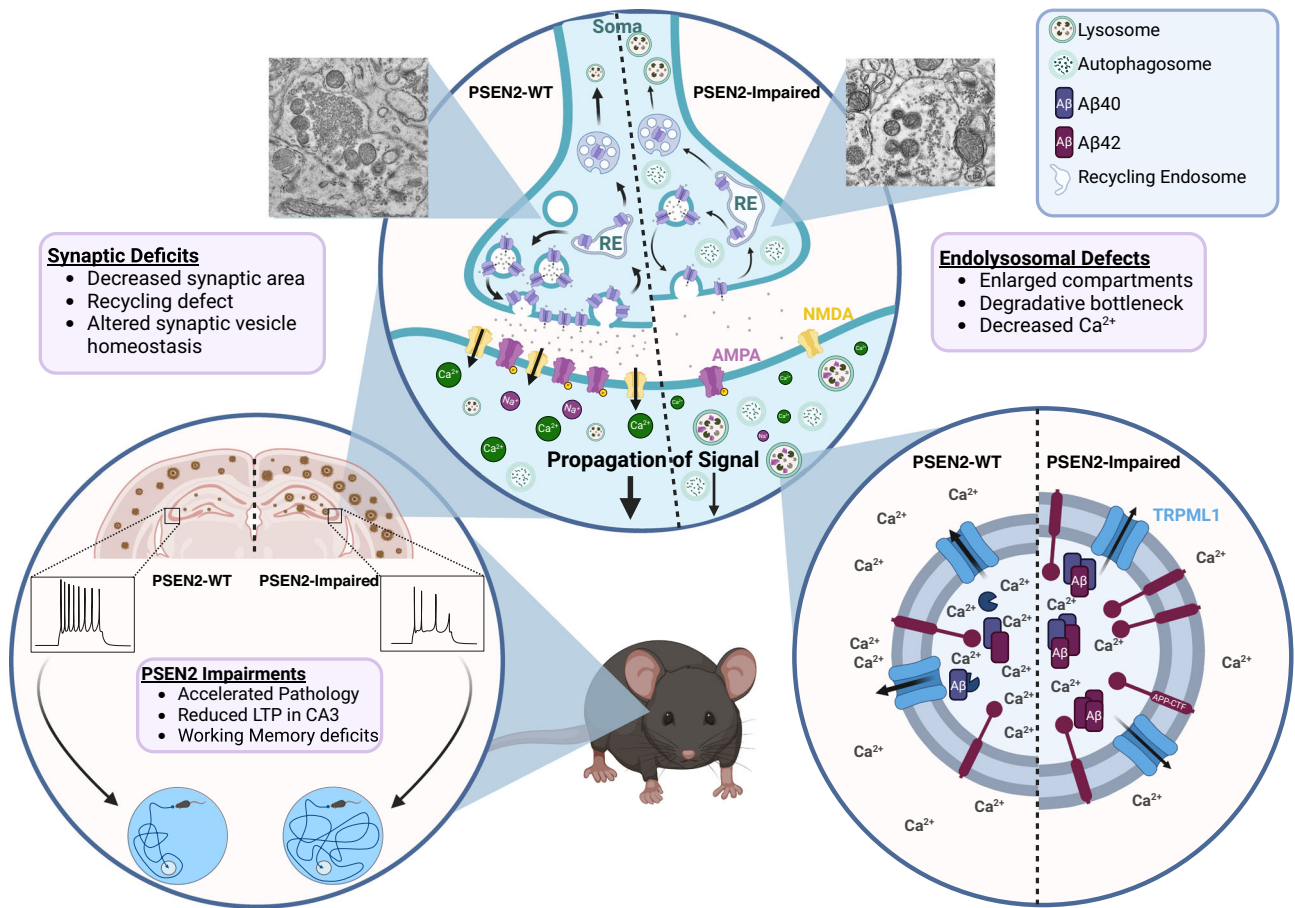


Fig. 8 | Altered PSEN2 expression impacts on synapse function and neuronal endolysosomal homeostasis. APPKI mice with altered PSEN2 expression present with increased pathology including plaques and dystrophic neurites. This leads to decreased LTP, specifically within the CA3 region of the hippocampus, impacting working memory. In vivo, mossy fiber synapses are reduced in size and display altered numbers of synaptic vesicles (only the APPxFADPSEN2 is displayed, showing reduced synaptic vesicle densities). In primary hippocampal neurons of

APPxPSEN2KO and APPxFADPSEN2, surface expression of GLUA1 and vGLUT1 is strongly lowered compared to APPKI, implying endosomal recycling defects. In these neurons, accumulation of enlarged LE/Lys, autophagosome and autolysosomes can be observed. LE/Lys have reduced basal Ca $^{2+}$ and Ca $^{2+}$ release upon stimulation of the TRPML-1, and accumulate APP metabolites, including APP-CTF and A β . Created in BioRender. Vrancx, C. (2024) <https://BioRender.com/s99m518>.

synaptic vesicle homeostasis. Mossy fiber synapses showed significant post-synaptic defects in all three genotypes compared to wild-type, but exacerbated in PSEN2-altered models. This defect between APPKI and wild type is not the case for the pre-synaptic compartment possibly indicating that mossy fiber PSDs are more vulnerable in disease. The effect of altered PSEN2 expression on pre-synapses is in line with reports that PSEN ablation mainly affects presynaptic components. PSENs have been studied extensively in synaptic signaling, with significant impairments observed when conditionally deleting both PSENs. Herein, LTP deficits were seen only in CA3, but not CA1 region

of PSEN double KO, indicating a pre-synaptic defect, likely mediated through decreased intracellular Ca $^{2+}$ affecting the replenishment of the ready releasable pool of synaptic vesicles^{69,102-105}. We noted LTP deficits solely in the CA3 region regardless of PSEN2KO or mutant PSEN2. In line with the alterations in synaptic vesicle clustering, APPxPSEN2KO showed synaptic facilitation in both paired-pulse and train stimulation paradigms, while APPxFADPSEN2 showed synaptic depression only upon CA3 stimulation. Though PSEN2KO and FADPSEN2 have similar effects on LTP, this occurs likely through different mechanisms that warrant further investigation.

In primary hippocampal neurons, altered PSEN2 expression lowered surface levels of presynaptic VGLUT1 and postsynaptic AMPARs, underscoring PSEN2-dependent defects in receptor recycling and degradation. Similarly, PSEN2 expression significantly affected LE/Lys homeostasis. Compared to APPKI neurons, PSEN2 deficiency and FADPSEN2 decreased LE/Lys basal Ca^{2+} levels, reduced TRPML1-dependent Ca^{2+} release and exocytosis, and led to accumulation of LC3^+ autophagosomes, as a proxy for defects in autophagy-lysosomal degradation. We believe this dysfunction stems from aberrant accumulation of APP metabolic products, i.e. APP-CTF and $\text{A}\beta$, in LE/Lys. While excess toxic $\text{A}\beta_{42}$ impairs synaptic function^{106–108}, the opposite effects on γ -secretase processivity between PSEN2KO and FADPSEN2, argues for additional mechanisms. Notably, both genotypes exhibited increased levels of APP-CTFs, increasingly connected to endolysosomal dysfunctions in AD pathology. Studies in iPSC-derived neurons harboring FAD-mutations in APP and/or PSEN1 identified APP- β CTF as a key perpetrator in endolysosomal and autophagic abnormalities^{63,64,109,110}. Further, phosphorylated APP- β CTF was found to also disrupt proton pump through binding to the V0a1 subunit⁶⁵. More recently, we found that excess APP-CTF impairs lysosomal Ca^{2+} refilling from the ER through LE/Lys-ER contact sites, explaining the decreased lysosomal Ca^{2+} in PSEN deficient models^{67,111} and in this study.

Endolysosomal defects, as those in our models, are strongly implicated in synaptic integrity. In lysosomal storage diseases, LE/Lys dysfunction impairs presynaptic integrity by disrupting lysosome-autophagy degradation and as such, synaptic vesicle recycling¹¹². This is reflected in decreased synaptic vesicle clustering¹¹³; a feature also seen in α -synuclein overexpression models for Parkinson's disease¹¹⁴ and reminiscent of FADPSEN2 MF synapses (Fig. 5). Both APPxPSEN2KO and APPxFADPSEN2 presented with similar lysosomal and autophagy defects. However, in a PSEN2KO background this resulted in more densely clustered synaptic vesicles, whereas more sparse in FADPSEN2 synapses. The appearance of larger vesicles may suggest underlying recycling defects in APPxPSEN2KO and APPxFADPSEN2 neurons as well. At the post-synapse, lysosomal Ca^{2+} release and lysosomal exocytosis, both decreased in PSEN2KO and FADPSEN2 neurons, are crucial for long-term structural plasticity, coupling GLUA1 activation to postsynaptic LE/Lys Ca^{2+} stores^{115,116}. Similarly, lysosomal Ca^{2+} regulates dendritic lysosome availability; defects herein impacted GLUA1 trafficking and lysosomal degradation, thus affecting LTP and synaptic plasticity^{117,118}. Further, Rab7-dependent transport from LE to somatic lysosomes is required for AMPAR degradation, and the partitioning of AMPARs to LE/Lys instead of recycling determines synaptic depression upon LTD induction^{119–121}. Interference with RAB7/LE function affects dendritic and axonal maintenance, with Rab7 mutations linked to Charcot-Marie Tooth disease type 2B resulting in axonal neuropathy¹²².

PSEN2 has been less studied in AD pathogenesis compared to the more prevalent mutated *PSEN1* and *APP* genes. Our study revealed the similar detrimental effects PSEN2KO and FADPSEN2 have on amyloid pathology and the endolysosomal system, with subsequent impacts on synaptic signaling (Fig. 8). PSEN2 deficiency exacerbated amyloid pathology, suggesting that PSEN2 expression might be protective in AD. In sporadic AD, splice variants in *PSEN2*, but not *PSEN1*, lead to truncated/lowered transcripts^{123,124}, indicating that PSEN2 loss-of-function may contribute to late onset AD. The worsening of amyloid pathology by PSEN2KO argues against therapeutically targeting individual γ -secretase complexes, but also that reducing $\text{iA}\beta$ pools or improving γ -secretase processivity alone may not be enough to delay disease progression. It would be interesting to extend this study to a humanized APP mouse model¹²⁵, as this would allow to investigate the direct potential of altered PSEN2 expression to induce amyloid pathology instead of the impact on existing amyloid pathology as investigated here. Another limitation is that our study did not address the role of altered PSEN2 expression

in microglia, but initial data show significant differences: PSEN2KO accelerated microglial recruitment to plaques whereas the N141I KI mutation delayed it compared to APP KI mice (Perdok et al., in preparation). We do not exclude that these outcomes may also relate to the observed plaque morphology differences (Fig. 2). PSEN2 has been suggested to mediate microglial inflammatory response^{126–128}. Many microglial activating proteins are type I transmembrane proteins, some of which are already identified as substrates¹²⁹, and the role of PSEN2-specific substrates in microglia is a focus of ongoing research. In conclusion, our study underscores the need to consider the contribution of individual γ -secretase complexes in AD pathogenesis to fully understand early molecular changes in AD pathology, which could be relevant for future therapeutic interventions.

Methods

The data generated in this study are provided in the Supplementary Information/Source Data file.

Experimental models

Mice. Mice carrying a FAD Psen2 mutation N141I were generated using CRISPR-Cas9 technology to target exon 6 of the mouse *Psen2* gene. Crispor webtool (<http://crispor.tefor.net/>) was used to select the guide RNA (5'CAUGAUGAGGGUGUUAAGCA), and efficiency of the guide RNA was tested in mouse embryonic fibroblasts (MEF). We made use of an ssODN carrying the mutated sequence in addition to three silent mutation within the PAM site and guide binding site (5' CAGCATCTACACGCCCTTACGGAGGACACGCCCTCGGTGGCCAGCGGCTCCTCAACTCTGTCTGATCACCTCATCATGATCAGCGTCATCGTAGTCATGACCATCTTCTCGTGGTACTCTACAA). Cas9 (50 ng/ μl), sgRNA (0.6 μM) and ssODN (12.5 ng/ μl) were injected into the pronucleus of C57BL/6J embryos via microinjection in collaboration with the Mouse Expertise Unit of KU Leuven. Positive pups were selected by PCR and Sanger Sequencing (Figure S1b, c) using the set of primers listed in Table 1.

Sanger sequencing confirmed the absence of unwanted additional mutations at the target site (608 bp amplicon FI-R1). One pup was selected as founder and backcrossed for two generations with C57BL/6J to cross out any potential unknown off-target in the founder mouse. PSEN2KO and APP NLGF (both in C57BL/6J) were kindly provided by Bart de Strooper and Takaomi Saido. Mice were housed under standard conditions, on a diurnal 14-hour light/dark cycle with ad libitum access to food and water. Only female mice were utilized for experiments. All experiments were approved by the KU Leuven ethical committee (ECDs: 174/2017, 173/2022, Creation Annaert Willem/2020).

Neuronal cultures. Cortical and hippocampal mouse neurons were obtained from randomly chosen male and female E17.5 embryos. Brain tissues were dissected and incubated in 0.25% trypsin in HBSS (10% HBSS, 1% HEPES, 1% Penicillin/Streptomycin, 0.5% NaHCO_3 in sterile water) for 15 min at 37 °C. Neurons were washed in memHorse (10% Horse serum, 1% Penicillin/Streptomycin, 1% GlutaMAX in MEM medium) followed by mechanical dissociation using flamed glass Pasteur pipettes. Individual neurons were counted using the Countess III and 250,000 neurons were plated in a 6 cm dish containing poly-L-lysine (PLL) coated 15 mm coverslips for imaging or 900,000 neurons on 6 cm PLL coated dishes for western blot. Subsequently, coverslips were flipped onto a glia feeding layer grown in Neurobasal medium supplemented with 2% B27 supplement, 1% Glutamax and 1% Penicillin/Streptomycin. Three days after the culture 5-Fluoro-2'-deoxyuridine (FDU) was added to prevent overgrowth of glia cells.

Antibodies and reagents. Mouse anti-human $\text{A}\beta$ (82e1, 10323, Tecan, 1:100 for IF, 1:500 for WB), anti-human $\text{A}\beta$ fibrils (AB2287, Sigma Aldrich, 1:200 for IF), rat anti-Lamp1 (1D4B, sc19992 Santa Cruz, 1:200 for IF, 1:1000 for WB), rabbit anti-APP (Y188, Ab32136, Abcam, 1:500 for

Table 1 | PCR and Sanger Sequencing primers

Combination	Primer	Sequence	PCR Product
I	3960_hPS2_N141I_ex6_F	GGAGCCTTTAATCCCTGT	615 bp
	3961_hPS2_N141I_ex6_R	GTATTAGGTCATCCACGGT	
II	3978_hPS2_N141I_WT_F	CTCAACTCCGTGCTGAA	266 bp
	3961_hPS2_N141I_ex6_R	GTATTAGGTCATCCACGGT	
III	3960_hPS2_N141I_ex6_F	GGAGCCTTTAATCCCTGT	378 bp
	3979_hPS2_N141I_WT_R	ATGATGAGGGTGTTCCAGC	
IV	3960_hPS2_N141I_ex6_F	GGAGCCTTTAATCCCTGT	266 bp (band only if CRISPR worked)
	3981_hPS2_N141I_mut_R	ATGATGAGGGTGATGAGG	
V	3980_hPS2_N141I_mut_F	CCTCAACTCCGTCCCTCAT	378 bp (band only if CRISPR worked)
	3961_hPS2_N141I_ex6_R	GTATTAGGTCATCCACGGT	

IF), rabbit anti-APP (B63.3, home-made, 1:10 000 for WB), rabbit anti-presenilin 2 (ab51249, abcam, 1:500 for IF, 1:10 000 for WB), rabbit anti-presenilin 1 (B19, home-made, 1:20 000 for WB), mouse anti-nicastrin (9C3, home-made, 1:8000 for WB), mouse anti-actin (A5441, Sigma Aldrich, 1:10 000 for WB), chicken anti-Map2 (PA1-10005, Thermo Fisher, 1:5000 for IF), rabbit anti-EEA1 (07-1820, Sigma Aldrich, 1:250 for IF), goat anti-VPS35 (ab10099, Abcam, 1:200 for IF), mouse anti-GLUA1 (MA5-27694, Invitrogen, 1:500 for IF, 1:1000 for WB), rabbit anti-pGLUA1 (p1160-845, Phosphosolutions, 1:100 for IF), guinea-pig anti-vGLUT1 (I35,304, Synaptic Systems, 1:500 for IF, 1:5000 for WB), PSD 95 nanobody-647 (N3702-AF647-L, Synaptic Systems, 1: 500 for IF), mouse anti-synaptobrevin2 (104 211, Synaptic Systems, 1:500 for IF), mouse anti-ankyrin-G coupled to FL550 (75-146-FL550, Neuro-Mab, 1:500).

Experimental methods

Immunohistochemistry. Mice were anaesthetized using xylazine/ketamine (Ketamine/Xylazine dosage: 0.1 ml/ 20 g intraperitoneal. Delivers: 87.5 mg/kg Ketamine/12.5 mg/kg Xylazine) and transcardially perfused using PBS (–/–). Mice were decapitated and brains were post-fixed for 48 h in 4% PFA. Coronal (60 μ m) free-floating sections were blocked using PBS –/– containing 3% goat serum and 0.3% Triton100x for 1.5 h at room temperature followed by overnight incubation at 4°C with the primary antibody. After three washes in PBS –/–, slices were incubated with Alexa-labelled secondary antibodies (1:500) for 2hrs at room temperature. In case of Thioflavin staining, slices were incubated in 0.05% Thioflavin for 5 min followed by two progressive dehydration steps in 70% and 90% ethanol, respectively. Finally, slices were washed three in PBS –/– and once in sterile water before mounting using ProLong Glass Antifade Mountant. Sections were visualized on a Nikon AIR Eclipse confocal system or Nikon AX. For analysis of brain slices, total area covered was always measured by delineating the cortex or the hippocampus and then calculating the area covered by the fluorescence staining of interest.

Neurons were fixed for 20 min at room temperature in 4% paraformaldehyde (PFA) and semi-permeabilized in 0.1% Triton X-100 in PBS for 5 min. In case of surface labelling of vGLUT1, GLUA1 and LAMP1, the permeabilization step was skipped, keeping the remaining procedure the same. Following a 1 h blocking step in blocking buffer (PBS + 2%BSA + 5%donkey or 5%goat serum) at room temperature, coverslips were incubated with primary antibody diluted in blocking buffer overnight at 4°C. Following three washes with PBS (+/+) coverslips were incubated with Alexa-labelled secondary antibodies (1:1000) at room temperature. Coverslips were mounted using ProLong Glass Antifade Mountant. Coverslips were imaged on a Zeiss LSM 900 and all image analysis was done using ImageJ.

Image quantification. All confocal image quantification was done using ImageJ.

PSD95 puncta: Two neuronal extensions were selected using a segmented line. Subsequently a rectangle was fit to the selection and duplicated from the original image. The length of the selected branch was measured followed by the number of PSD95 puncta using thresholding with the default mask. The total number of puncta was divided by the length of the segment to obtain puncta per μ m and the average size of puncta per neuron was taken to investigate PSD size.

Surface labelling vGLUT1, GLUA1 and LAMP1: The phalloidin channel was used to determine total cell surface with thresholding using the MaxEntropy mask and total area measured. This mask was then applied to the vGLUT1, GLUA1 or LAMP1 channel and everything outside the mask was subtracted to remove non-specific staining. Subsequently, the total area of surface protein was determined with thresholding using the MaxEntropy mask and next divided by cell area to derive a % of total surface covered by the respective protein.

Compartment size: The soma of the neuron was delineated, the size measured and everything outside the soma removed. Then the total area of LAMP1, EEA1 and VPS35 immunostaining was delineated using thresholding with the MaxEntropy mask. The total compartment area was divided by soma area to get a %soma area covered by the cellular compartment.

Triple overlap: Overlap of three different channels in the case of LAMP1 and Y188/82e1 and PSD95 and PSEN2/LAMP1 immunoreactivities were measured using the ComDet v.0.5.5. plugin in Fiji. Max distance between colocalized spots was set at 10 pixels, with the approximate particle size as 20 pixels and an intensity threshold of 5.

Biochemical sample collection. Mice were transcardially perfused and brains were extricated from the skull. Cerebrum and hippocampi were flash frozen, separately, using liquid nitrogen and stored at –70°C until further use. Tissue samples were weighed and homogenized using a FastPrep bead mill in T-PER™ Tissue Protein Extraction Reagent (78510, Thermo Scientific). Beads were spun down and supernatants centrifuged for one hour at 263,000 \times g at 4°C. Supernatants were kept as soluble fraction and the pellet was further resuspended in 2 volumes 6 M Guanidine buffer (G3272-100G, Sigma-Aldrich) sonicated and vortexed followed by a one-hour incubation at 25°C. Samples were centrifuged for 20 min at 426,204 \times g and the obtained supernatant diluted 12x in guanidine diluent (20 mM phosphate, 0.4 M NaCl, 2 mM EDTA, 10% Block Ace, 0.2% BSA, 0.05% Na₃N, 0.075% CHAPS, protease inhibitor cocktail, pH 7.0). Samples were stored at –70 until further use.

Western blot. Protein concentrations were determined using the Bio-Rad Protein Assay Dye Reagent (5000006, Bio-Rad). Samples of equal protein content were heated in 4x loading buffer (NuPage LDS Samples Buffer 4x, NP0008, Invitrogen) at 70°C for 10 min, loaded in NuPage 4%–12%, Bis-Tris gels (NP0322BOX, Invitrogen) and separated by electrophoresis in NuPage SDS MES running buffer (NP0002,

Invitrogen). Proteins were transferred to nitrocellulose membranes (Life technologies) for 2 h at 4 °C. Membranes were subsequently blocked in 5% non-fat milk powder dissolved in TBS containing 0.1% Tween 20 (TBS-T; blocking buffer) for 1 h at room temperature followed by overnight incubation in primary antibody diluted in blocking buffer at 4 °C. Following incubation, membranes were washed in TBS-T and incubated with horseradish peroxidase-conjugated secondary antibody (1:10 000) diluted in blocking buffer for 1 h at room temperature. Following washing in TBS-T membranes were incubated with Western Lighting Plus-ECL (NEL105001EA, Perkin Elmer) and protein bands were visualized and images by chemiluminescence in a IQ680. Images were analyzed and quantified using Aida Image Analyzer software (Raytest, Germany).

ELISA. To quantify the concentration of A β 37, A β 38, A β 40 and A β 42 peptides, MesoScale Discovery (MSD) multispot A β ELISA plates pre-coated with anti- A β 37, A β 38, A β 40 and A β 42 was used. In case of brain extracts, the soluble fraction was undiluted and insoluble fractions were diluted 1:200 in blocking buffer (PBS + 0.1% casein). For neuron extracts, 12 μ g protein was used for the intracellular fraction (diluted in blocking buffer) and the secreted pool was diluted 1:2 in blocking buffer. Plates were blocked with blocking buffer (PBS + 0.1% casein) for 2 h at room temperature. SULFO-TAG JRF/AbN/25 detection antibody was diluted 1:1 with standards (synthetic human A β 37, A β 38, A β 40 and A β 42 peptides of known concentration) or with prepared samples. 50 μ l of the mix was added to the wells and incubated overnight at 4 °C. After incubation, plates were washed 5x in washing buffer and signal was developed by adding 150 μ l/well of the 2x MSD Read Buffer T (Tris-based buffer containing tripropylamine). Plate was read Sector Imager 6000 (Meso Scale Discovery).

Transfection of hippocampal neurons. Coverslips were placed in a 12well plate containing 200 μ l conditioned medium and 50 μ l 5x kynurenic acid (final concentration 2 mM, K3375-250MG, Sigma-Aldrich). Per coverslip 100 μ l of precipitate was prepared by diluting 2 μ g of plasmid (mCherry-GFP-LC3 ref: 10.1186/s13024-017-0165-0) in 1x TE buffer (10 μ M Tris-HCl pH 7.5, 5 mM EDTA pH 8, adjusted to pH 7.3) to a final volume of 45 μ l mixing gently, and followed by the addition of 5 μ l of 2.5 M CaCl₂ and mixing gently. Finally, 50 μ l of 2x HEBS buffer (NaCl, KCl, Na₂HPO₄, Glucose, HEPES) are added and the precipitate is mixed and added dropwise to the coverslips. Coverslips are incubated for 2 h at 37 °C and 5%CO₂ following by a 15 min wash in acidic 5% CO₂ equilibrated wash medium (200 μ l 5x kynurenic acid and 800 μ l Neurobasal medium per coverslip). Coverslips were transferred to their original dish and fixed or imaged 48 h after transfection. Live imaging was performed using the LSM880 or LSM980 using the fast Airyscan mode taking 10 images with the lowest interval possible. The 488 nm and 543 nm lasers were used to image the GFP and mCherry channels respectively. For analysis, Fiji was used. Images were max projected and subsequently the number of red and yellow puncta were manually quantified.

TRPML1-dependent lysosomal calcium release. Lysosomal Ca²⁺ release was measured as previously stated¹³⁰. Briefly, cells were incubated with 1 μ M Fura-2 AM solution (F1221, Thermo Fisher Scientific) for 45 min at room temperature in the dark. Cells were rinsed twice with Krebs-Ca²⁺ (135 mM NaCl, 5.9 mM KCl, 11.5 mM Glucose, 11.6 mM HEPES, 1.2 mM MgCl₂, and 1.5 mM CaCl₂) and left at room temperature for 30 min for de-esterization, in the dark. All acquisitions were carried out in Krebs-EGTA⁺ (135 mM NaCl, 5.9 mM KCl, 11.5 mM Glucose, 11.6 mM HEPES, 1.2 mM MgCl₂, and 2 mM EGTA). A baseline Fura-2 signal was measured for 30 s followed by a pulse with 20 μ M of the TRPML agonist ML-SA1 (Cat. No. 4746, Tocris) and the response was acquired every 5 s for 10 min, using an Olympus IX81 with a UAPO/340 40x oil objective (1.35 NA) and operated by CellR Software (Olympus). Recordings were done at 340 and 380 nm excitation (530 nm emission

filters). For image analysis, regions were segmented manually in Image J and fluorescence intensities were measured over time. Fura-2 signals were corrected to obtain $\Delta F/F_0$ (F_0 being the initial signal recorded). In addition, each cell's area under the curve was measured using Prism GraphPad (Version 10.02).

Rhodamine dextran lysosomal calcium assay. Coverslips with DIV14 hippocampal neurons were placed in a 12-well plate and Rhodamine (0.25 mg/ml, 20451-1 mg, AAT Bioquest) and Dextran-488 (0.1 mg/ml, D22910, ThermoFisher) diluted in conditioned medium were added for 8 h. Neurons were washed twice in medium and returned to their original dish for an overnight chase. The day after neurons were washed twice in HBSS (+/+) without phenol red and imaged live on the LSM880 or LSM980 using the fast Airyscan mode taking a single snap shot using the 488 nm and 543 nm lasers. For analysis, lysosomes were delineated by generating a mask using the green channel and the average green intensity was measured. Then the average red channel intensity was measured within the lysosomal mask to determine levels of lysosomal calcium.

Electrophysiology. Mice were anesthetized with isoflurane and brains were dissected and transferred into ice-cold cutting solution (87 mM NaCl, 2.5 mM KCl, 1.25 mM NaH₂PO₄, 10 mM glucose, 25 mM NaHCO₃, 0.5 mM CaCl₂, 7 mM MgCl₂, 75 mM sucrose, 1 mM kynurenic acid, 5 mM ascorbic acid and 3 mM pyruvic acid) at pH 7.4 and 5% CO₂/95% O₂. 300 μ m-thick parasagittal hippocampal sections were incubated at 34 °C for 35 min to recover. For recordings, slices were placed onto a multielectrode array (MEA 2100, Multichannel Systems) and continuously perfused with prewarmed (33–34 °C) artificial cerebrospinal fluid (aCSF; 119 mM NaCl, 2.5 mM KCl, 1 mM NaH₂PO₄, 11 mM glucose, 26 mM NaHCO₃, 4 mM MgCl₂ and 4 mM CaCl₂) at pH 7.4, 95% O₂ and 5% CO₂. Field excitatory post-synaptic potentials (fEPSPs) were recorded from mossy fiber-CA3 synapses by stimulating and recording from the appropriate (visually identified) electrodes. Input-output curves were established for each individual slice by applying single stimuli ranging from 500 to 2750 mV with 250 mV increments. Stimulus strength that corresponds to 35% of maximal response in the input-output curve was applied for the following recordings. For long-term potentiation (LTP) experiments, stable fEPSPs were recorded for 30 min as baseline. Next, two trains of high-frequency stimulation (75 stimuli, 100 Hz) with 5 min interval were applied to induce LTP and consecutive fEPSPs were recorded for 55 additional minutes. Baseline and post-LTP induction fEPSPs were recorded every 5 min using three consecutive stimulations, 15 s apart. These triplets were averaged during analysis. For paired pulse and train stimulations we used separate, naïve slices. Slices were continuously perfused with prewarmed (33–34 °C) artificial cerebrospinal fluid (aCSF; 127 mM NaCl, 2.5 mM KCl, 1.25 mM NaH₂PO₄, 25 mM glucose, 25 mM NaHCO₃, 1 mM MgCl₂ and 2 mM CaCl₂) at pH 7.4, 95% O₂ and 5% CO₂. Input-output curves as described above were used to determine stimulation strength required for 35% maximal response. Three repetitions of each paired pulse stimulation (inter-stimulation intervals: 20, 40, 60, 80, 100, 200, 400, 800, 1000 and 2000 ms) were recorded and averaged (1 minute between pairs). For train stimulations we recorded and averaged two repetitions for each train (1, 5, 10 and 20 Hz; 10 stimulations; 5 min between trains). Recordings were analyzed and processed using Multi Channel Experimenter software (Multichannel Systems).

Imaging

Transmission electron microscopy. Mice were anaesthetized using xylazine/ketamine and transcardially perfused using PBS (–/–) following perfusion with fixative solution (4% paraformaldehyde, 2.5% glutaraldehyde and 0.2% picric acid in 0.1 M Phosphate Buffer) and brains were dissected and post-fixed in fixative solution overnight at 4 °C. Subsequently, brains were washed in 0.1 M Phosphate Buffer,

embedded in 3% agarose (Sigma-Aldrich) and 100 μ m-thick coronal sections were cut using a vibratome (VT1000S, Leica). Hippocampal CA3 regions were cropped from the brain sections and left overnight in 0.1 M PB buffer. Cropped sections were washed on ice first in 0.1 M PB buffer followed by double distilled water (ddH₂O) washes and then were post-fixed in 0.1 M Phosphate Buffer containing 1% OsO₄ and 1.5% K₄Fe(CN)₆ for one hour at on ice in the dark. Following washing in ddH₂O, sections were incubated with 0.2% tannic acid in ddH₂O for 30 min in the dark at room temperature followed by an additional incubation in 1% OsO₄ in the dark. Following washing step cropped sections are incubated overnight in 25% methanol with 0.5% uranyl acetate overnight at 4 °C with rotation in the dark. After, sections were washed in ddH₂O and incubated with Walton's lead aspartate (0.02 M lead nitrate in 0.03 M sodium aspartate, pH 5.5) for 30 min at 60 °C, washed again in ddH₂O and dehydrated with graded series of ethanol (30%, 50%, 70%, 80%, 95% and 100%). Following two washes in 100% ethanol and two washes in propylene oxide, sections were infiltrated with different ratios of propylene oxide:resin (2:1, 1:1 and 1:2 supplemented with BDMA) and embedded in pure EPON resin (supplemented with BDMA). Ultrathin 70 nm-thick sections were cut using an ultramicrotome (EM UC7, Leica) and collected on copper grids. Images of mossy fiber-CA3 synapses were acquired with a JEOL JEM1400 transmission electron microscope equipped with an Olympus SIS Quemesa camera with 4000X or 25000X magnification. Images were analyzed using Microscopy Image Browser (MIB, University of Helsinki)¹³¹ and processed using Fiji software (National Institutes of Health).

Behavior. All animal behavioral experiments were performed at and in collaboration with the mINT Animal Behavior Facility at the KU Leuven Faculty of Psychology. Mice were transferred 10 days prior to tested for acclimatization.

24 h activity. Mice were caged individually with ad libitum access to food and water. Cages were placed centrally between 3 lasers and laser crossings were monitored overnight. For analysis, total laser crossings were summated for each hour to indicate overall activity.

Open field. Anxiety and locomotor activity were tested using an open field paradigm. Prior to testing, mice were housed in the dark for 30 min. Then mice were placed in a square box constructed from plexiglass and tracked for 10 min using an over-head camera and ANY-maze tracking software (Stölting). Time spend in the middle was compared as an indication for anxiety and total distance travelled as a readout for locomotion.

Elevated plus maze. Anxiety was tested using the elevated plus maze apparatus consisting of two open arms and two closed arms, elevated 50 cm off the ground. Mice were placed in the center tracked for 10 min using an over-head camera and ANY-maze tracking software (Stölting). Time spend in the open arms versus close arms was measured as readout for anxiety-like behavior.

Social novelty/social preference. Social memory was tested in a three-chamber setup constructed from plexiglass¹³². The test mouse was placed in the central chamber which is connected by two walls containing 8 mm holes allowing for the exchange of olfactory, visual, and auditory signals. Following a 5 min habituation period, a novel mouse of the same gender was placed in one of the adjacent chambers (S1) and the preference of the test mouse to approach the novel mouse over the empty chamber was measured. After 10 min, a second stranger mouse was placed in the opposing chamber (S2) and social memory was tested as preference of the new mouse over the old mouse. Animals were tracked using an overhead camera and ANY-maze tracking software (Stölting). Time

sniffing (head within 5 cm of the separation wall) was compared between groups.

Morris water maze. Spatial learning was tested in a hidden platform protocol in the Morris Water Maze¹³³. Mice were trained to locate a hidden platform (15 cm in diameter) in a pool (150 cm in diameter) filled with opaque water (26 ± 1 °C) surrounded by spatial cues. Mice were placed in the pool 4 times per day, from different entry points, for a maximum of 100 s during which the mouse is tracked using an overhead camera and Ethovision software (Noldus, Wageningen, NL). On training day 6 and 11 a probe the platform was removed from the pool and the time spend in the target quadrant was observed indicative of spatial learning.

Delayed matching to platform. Following the Morris Water Maze protocol, mice were subjected to an altered protocol to test working memory. Herein the platform location was altered every day. Mice were placed in the pool 4 times per day, from different entry points opposing the new location of the platform. Mouse was tracked using the same software and parameters as during the Morris Water Maze protocol. For analysis, the distances for the different swims were averaged over the week to observe decreases, indicative of a functional working memory.

Statistics, image analysis and reproducibility. For image analysis the freely available software ImageJ was used. Graphical and statistical analysis was done using GraphPad (Version 10.02). Statistical tests used are specified in the figure legends. For all experiments, data were reported based on individual cells/animals or biological replicates pooled from multiple cells, e.g. lysates. No statistical methods were used to predetermine the sample size. Further information on research design is available in the Nature Portfolio Reporting Summary linked to this article.

Reporting summary

Further information on research design is available in the Nature Portfolio Reporting Summary linked to this article.

Data availability

All data are available in the main text or the supplementary materials. Source data are provided with this paper. The data is further available from the corresponding author upon request. Source data are provided with this paper.

References

1. Jurisch-Yaksi, N., Sannerud, R. & Annaert, W. A fast growing spectrum of biological functions of γ -secretase in development and disease. *Biochim Biophys. Acta Biomembr.* **1828**, 2815–2827 (2013).
2. Güner, G. & Lichtenthaler, S. F. The substrate repertoire of γ -secretase/presenilin. *Semin Cell Dev. Biol.* **105**, 27–42 (2020).
3. De Strooper, B. et al. A presenilin-1-dependent γ -secretase-like protease mediates release of notch intracellular domain. *Nature* **398**, 518–522 (1999).
4. Struhl, G. & Greenwald, I. Presenilin is required for activity and nuclear access of Notch in Drosophila. *Nature* **398**, 522–524 (1999).
5. Hartmann, D., De Strooper, B. & Saftig, P. Presenilin-1 deficiency leads to loss of Cajal-Retzius neurons and cortical dysplasia similar to human type 2 lissencephaly. *Curr. Biol.* **9**, 719–727 (1999).
6. Wolfe, M. S. et al. A substrate-based difluoro ketone selectively inhibits Alzheimer's γ -secretase activity. *J. Med. Chem.* **41**, 6–9 (1998).
7. De Strooper, B. Aph-1, Pen-2, and Nicastrin with Presenilin generate an active γ -Secretase complex. *Neuron* **38**, 9–12 (2003).

8. Takasugi, N. et al. The role of presenilin cofactors in the γ -secretase complex. *Nature* **422**, 438–441 (2003).
9. Escamilla-Ayala A., Wouters R., Sannerud R., Annaert W. Contribution of the Presenilins in the cell biology, structure and function of γ -secretase. *Semin Cell Dev Biol.* **105**, 12–26 (2020).
10. Hebert S. S., et al. Coordinated and widespread expression of γ -secretase in vivo: evidence for size and molecular heterogeneity. *Neurobiol Dis* **17**, 260–272 (2004).
11. Takami, M. et al. Secretase: Successive tripeptide and tetrapeptide release from the transmembrane domain of β -carboxyl terminal fragment. *J. Neurosci.* **29**, 13042–13052 (2009).
12. Szaruga, M. et al. Alzheimer's-Causing Mutations Shift A β Length by Destabilizing γ -Secretase-A β n Interactions. *Cell* **170**, 443–456.e14 (2017).
13. Funamoto, S. et al. Truncated carboxyl-terminal fragments of β -amyloid precursor protein are processed to amyloid β -proteins 40 and 42. *Biochemistry* **43**, 13532–13540 (2004).
14. Hardy, J. A. & Higgins, G. A. Alzheimer's Disease: The Amyloid Cascade Hypothesis. *Science.* **256**, 184–185 (1992).
15. Hardy, J. & Selkoe, D. J. The amyloid hypothesis of Alzheimer's disease: Progress and problems on the road to therapeutics. *Science.* **297**, 353–356 (2002).
16. Shen, J. et al. Skeletal and CNS Defects in Presenilin-1-Deficient mice. *Cell* **89**, 629–639 (1997).
17. De Strooper, B. et al. Deficiency of presenilin-1 inhibits the normal cleavage of amyloid precursor protein. *Nature* **391**, 387–390 (1998).
18. Herreman, A. et al. Presenilin 2 deficiency causes a mild pulmonary phenotype and no changes in amyloid precursor protein processing but enhances the embryonic lethal phenotype of presenilin 1 deficiency. *Proc. Natl Acad. Sci. USA.* **96**, 11872–11877 (1999).
19. Steiner, H. et al. A loss of function mutation of presenilin-2 interferes with amyloid β -peptide production and Notch signaling. *J. Biol. Chem.* **274**, 28669–28673 (1999).
20. Donoviel, D. B. et al. Mice lacking both presenilin genes exhibit early embryonic patterning defects. *Genes Dev.* **13**, 2801–2810 (1999).
21. Acx, H. et al. Inactivation of γ -secretases leads to accumulation of substrates and non-Alzheimer neurodegeneration. *EMBO Mol. Med.* **9**, 1088–1099 (2017).
22. Faguás, C. M. S., Molina, P. S. & Saura, C. A. Loss of presenilin function enhances tau phosphorylation and aggregation in mice. *Acta Neuropathol. Commun.* **7**, 1–20 (2021).
23. Peethumongsin, E. et al. Convergence of presenilin- and tau-mediated pathways on axonal trafficking and neuronal function. *J. Neurosci.* **30**, 13409–13418 (2010).
24. Saura, C. A. et al. Loss of presenilin function causes impairments of memory and synaptic plasticity followed by age-dependent neurodegeneration. *Neuron* **42**, 23–36 (2004).
25. Watanabe, H., Iqbal, M., Zheng, J., Wines-Samuelson, M. & Shen, J. Partial loss of presenilin impairs age-dependent neuronal survival in the cerebral cortex. *J. Neurosci.* **34**, 15912–15922 (2014).
26. Beglopoulos, V. et al. Reduced β -amyloid production and increased inflammatory responses in presenilin conditional knock-out mice. *J. Biol. Chem.* **279**, 46907–46914 (2004).
27. Jayadev, S. et al. Alzheimer's disease phenotypes and genotypes associated with mutations in presenilin 2. *Brain* **133**, 1143–1154 (2010).
28. Walker, E. S., Martinez, M., Brunkan, A. L. & Goate, A. Presenilin 2 familial Alzheimer's disease mutations result in partial loss of function and dramatic changes in A β 42/40 ratios. *J. Neurochem.* **92**, 294–301 (2005).
29. Sannerud, R. et al. Restricted Location of PSEN2/ γ -Secretase Determines Substrate Specificity and Generates an Intracellular A β Pool. *Cell* **166**, 193–208 (2016).
30. Petit, D. et al. A β profiles generated by Alzheimer's disease causing PSEN1 variants determine the pathogenicity of the mutation and predict age at disease onset. *Mol. Psychiatry* **27**, 2821–2832 (2022).
31. Meckler, X. & Checler, F. Presenilin 1 and presenilin 2 target γ -secretase complexes to distinct cellular compartments. *J. Biol. Chem.* **291**, 12821–12837 (2016).
32. Gouras, G. K. et al. Intraneuronal A β 42 accumulation in human brain. *Am. J. Pathol.* **156**, 15–20 (2000).
33. Billings, L. M. et al. causes the onset of early Alzheimer's disease-related cognitive deficits in transgenic mice. *Neuron* **45**, 675–688 (2005).
34. Gyure, K. A. et al. β -amyloid precedes development of amyloid plaques in Down syndrome. *Arch. Pathol. Lab Med.* **125**, 489–492 (2001).
35. Pensalfini, A. et al. Intracellular amyloid and the neuronal origin of Alzheimer neuritic plaques. *Neurobiol. Dis.* **71**, 53–61 (2014).
36. Su, Y. & Chang, P. T. Acidic pH promotes the formation of toxic fibrils from β -amyloid peptide. *Brain Res.* **893**, 287–291 (2001).
37. Liu, R. Q. et al. Membrane localization of β -amyloid 1-42 in lysosomes: A possible mechanism for lysosome labilization. *J. Biol. Chem.* **285**, 19986–19996 (2010).
38. Esbjörner, E. K. et al. Direct observations of amyloid β Self-assembly in live cells provide insights into differences in the kinetics of A β (1-40) and A β (1-42) aggregation. *Chem. Biol.* **21**, 732–742 (2014).
39. Yang, A. J., Chandswangbhuvana, D., Margol, L. & Glabe, C. G. Loss of endosomal/lysosomal membrane impermeability is an early event in amyloid A β 1-42 pathogenesis. *J. Neurosci. Res.* **52**, 691–698 (1998).
40. Friedrich, R. P. et al. Mechanism of amyloid plaque formation suggests an intracellular basis of A β pathogenicity. *Proc. Natl Acad. Sci. USA.* **107**, 1942–1947 (2010).
41. Brunello, L. et al. Presenilin-2 dampens intracellular Ca²⁺ stores by increasing Ca²⁺ leakage and reducing Ca²⁺ uptake. *J. Cell Mol. Med.* **13**, 3358–3369 (2009).
42. Fedeli, C., Filadi, R., Rossi, A., Mammucari, C. & Pizzo, P. PSEN2 (presenilin 2) mutants linked to familial Alzheimer disease impair autophagy by altering Ca²⁺ homeostasis. *Autophagy* **15**, 2044–2062 (2019).
43. Nuriel, T. et al. The endosomal-lysosomal pathway is dysregulated by APOE4 expression in vivo. *Front Neurosci.* **11**, 1–12 (2017).
44. Bustos, V. et al. Phosphorylated Presenilin 1 decreases β -amyloid by facilitating autophagosome-lysosome fusion. *Proc. Natl Acad. Sci. USA.* **114**, 7148–7153 (2017).
45. Cataldo, A. M. et al. Endocytic pathway abnormalities precede amyloid β deposition in sporadic Alzheimer's disease and Down syndrome: Differential effects of APOE genotype and presenilin mutations. *Am. J. Pathol.* **157**, 277–286 (2000).
46. Nixon, R. A. The role of autophagy in neurodegenerative disease. *Nat. Med.* **19**, 983–997 (2013).
47. Peric, A. & Annaert, W. Early etiology of Alzheimer's disease: tipping the balance toward autophagy or endosomal dysfunction? *Acta Neuropathol.* **129**, 363–381 (2015).
48. Saito, T. et al. Single App knock-in mouse models of Alzheimer's disease. *Nat. Neurosci. [Internet].* **17**, 661–663, <https://www.nature.com/articles/nn.3697> (2014).
49. Ueno, H. et al. Comparison between the aggregation of human and rodent amyloid β -proteins in GM1 ganglioside clusters. *Biochemistry* **53**, 7523–7530 (2014).
50. Boon, B. D. C. et al. The coarse-grained plaque: a divergent A β plaque-type in early-onset Alzheimer's disease. *Acta Neuropathol.* **140**, 811–830 (2020).

51. Gowrishankar, S. et al. Massive accumulation of luminal protease-deficient axonal lysosomes at Alzheimer's disease amyloid plaques. *Proc. Natl Acad. Sci. USA*. **112**, E3699–E3708 (2015).
52. Calafate, S. et al. Early alterations in the MCH system link aberrant neuronal activity and sleep disturbances in a mouse model of Alzheimer's disease. *Nat. Neurosci.* **26**, 1021–1031 (2023).
53. Morris, R. G. & Baddeley, A. D. Primary and Working Memory Functioning in Alzheimer-type Dementia. *J. Clin. Exp. Neuropsychol.* **10**, 279–296 (1987).
54. Stopford, C. L., Thompson, J. C., Neary, D., Richardson, A. M. T. & Snowden, J. S. Working memory, attention, and executive function in Alzheimer's disease and frontotemporal dementia. *Cortex* **48**, 429–446 (2012).
55. Adams, J. P. & Dudek, S. M. Late-phase long-term potentiation: getting to the nucleus. *Nat. Rev. Neurosci.* **6**, 737–743 (2005).
56. Baltaci, S. B., Mogulkoc, R., Baltaci, A. K. Molecular Mechanisms of Early and Late LTP. Vol. 44, Neurochemical Research. Springer New York LLC. 281–296 (2019).
57. Rollenhagen, A. & Lübke, J. H. R. The mossy fiber bouton: The “common” or the “unique” synapse? *Front. Synaptic Neurosci.* **2**, 1–9 (2010).
58. Díaz-Alonso, J. & Nicoll, R. A. AMPA receptor trafficking and LTP: Carboxy-termini, amino-termini and TARPs. *Neuropharmacology* **197**, 108710 (2021).
59. Fernández-Alfonso, T. & Ryan, T. A. The efficiency of the synaptic vesicle cycle at central nervous system synapses. *Trends Cell Biol.* **16**, 413–420 (2006).
60. Takahashi, R. H. et al. Intraneuronal Alzheimer A β 42 accumulates in multivesicular bodies and is associated with synaptic pathology. *Am. J. Pathol.* **161**, 1869–1879 (2002).
61. Almeida, C. G., Takahashi, R. H. & Gouras, G. K. B-Amyloid Accumulation Impairs Multivesicular Body Sorting By Inhibiting the Ubiquitin-Proteasome System. *J. Neurosci.* **26**, 4277–4288 (2006).
62. Hu, X. et al. Amyloid seeds formed by cellular uptake, concentration, and aggregation of the amyloid-beta peptide. *Proc. Natl Acad. Sci. USA*. **106**, 20324–20329 (2009).
63. Kwart, D. et al. A Large Panel of Isogenic APP and PSEN1 Mutant Human iPSC Neurons Reveals Shared Endosomal Abnormalities Mediated by APP β -CTFs, Not A β . *Neuron* **104**, 256–270.e5 (2019).
64. Hung, C. et al. SORL1 deficiency in human excitatory neurons causes APP-dependent defects in the endolysosome-autophagy network. *Cell Rep.* **35**, 109259 (2021).
65. Im, E. et al. Lysosomal dysfunction in Down syndrome and Alzheimer mouse models is caused by v-ATPase inhibition by Tyr682-phosphorylated APP β CTF. *Sci Adv.* **9**, eadg1925 (2023).
66. Saftig, P. & Klumperman, J. Lysosome biogenesis and lysosomal membrane proteins: Trafficking meets function. *Nat. Rev. Mol. Cell Biol.* **10**, 623–635 (2009).
67. Bretou, M. et al. Accumulation of APP C-terminal fragments causes endolysosomal dysfunction through the dysregulation of late endosome to lysosome-ER contact sites. *Dev. Cell.* **59**, 1571–1592.e9 (2024).
68. Essayan-Perez, S. & Südhof, T. C. Neuronal γ -secretase regulates lipid metabolism, linking cholesterol to synaptic dysfunction in Alzheimer's disease. *Neuron* **111**, 3176–3194 (2023).
69. Lee, S. H., Bolshakov, V. Y. & Shen, J. Presenilins regulate synaptic plasticity in the perforant pathways of the hippocampus. *Mol. Brain.* **16**, 1–12 (2023).
70. Chavez-Gutiérrez, L. et al. The mechanism of γ -Secretase dysfunction in familial Alzheimer disease. *EMBO J.* **31**, 2261–2274 (2012).
71. Braak, H., Thal, D. R., Ghebremedhin, E. & Del Tredici, K. Stages of the pathologic process in Alzheimer disease: Age categories from 1 to 100 years. *J. Neuropathol. Exp. Neurol.* **70**, 960–969 (2011).
72. Richards, J. G. et al. PS2APP transgenic mice, coexpressing hPS2mut and hAPP^{sw}, show age-related cognitive deficits associated with discrete brain amyloid deposition and inflammation. *J. Neurosci.* **23**, 8989–9003 (2003).
73. Toda, T., Noda, Y., Ito, G., Maeda, M. & Shimizu, T. Presenilin-2 mutation causes early amyloid accumulation and memory impairment in a transgenic mouse model of Alzheimer's disease. *J. Biomed. Biotechnol.* **2011**, 1–13 (2011).
74. Watanabe, H. et al. Flexible and accurate substrate processing with distinct presenilin/ γ -secretases in human cortical neurons. *eNeuro* **8**, 1–20 (2021).
75. Nilsberth, C. et al. The “Arctic” APP mutation (E693G) causes Alzheimer's disease by enhanced A β protofibril formation. *Nat. Neurosci.* **4**, 887–893 (2001).
76. Yang, Y. et al. Cryo-EM structures of amyloid-b 42 filaments from human brains. *Science*. **375**, 167–172 (2022).
77. Dickson, T. C. & Vickers, J. C. The morphological phenotype of β -amyloid plaques and associated neuritic changes in Alzheimer's disease. *Neuroscience* **105**, 99–107 (2001).
78. Thal, D. R., Walter, J., Saïdo, T. C. & Fändrich, M. Neuropathology and biochemistry of A β and its aggregates in Alzheimer's disease. *Acta Neuropathol.* **129**, 167–182 (2015).
79. Verkoniemi, A. et al. Variant Alzheimer's disease with spastic paraparesis: Clinical characterization. *Neurology* **54**, 1103–1109 (2000).
80. Le, T. V., Crook, R., Hardy, J. & Dickson, D. W. Cotton wool plaques in non-familial late-onset Alzheimer disease. *J. Neuropathol. Exp. Neurol.* **60**, 1051–1061 (2001).
81. Whyte, L. S. et al. Reduction in open field activity in the absence of memory deficits in the AppNL-G-F knock-in mouse model of Alzheimer's disease. *Behavioural Brain Res.* **336**, 177–181 (2018).
82. Mehla, J. et al. Age-dependent behavioral and biochemical characterization of single APP knock-in mouse (APPNL-G-F/NL-G-F) model of Alzheimer's disease. *Neurobiol. Aging* **75**, 25–37 (2019).
83. Latif-Hernandez, A. et al. Subtle behavioral changes and increased prefrontal-hippocampal network synchronicity in APP NL-G-F mice before prominent plaque deposition. *Behavioural Brain Res.* **364**, 431–441 (2019).
84. Salesse, C. et al. Opposite Control of Excitatory and Inhibitory Synapse Formation by Slitrk2 and Slitrk5 on Dopamine Neurons Modulates Hyperactivity Behavior. *Cell Rep.* **30**, 2374–2386.e5 (2020).
85. Busche, M. A. & Konnerth, A. Neuronal hyperactivity - A key defect in Alzheimer's disease? *BioEssays* **37**, 624–632 (2015).
86. Shah, D. et al. Astrocyte calcium dysfunction causes early network hyperactivity in Alzheimer's disease. *Cell Rep.* **40**, 111280 (2022).
87. Kipanyula, M. J. et al. Ca²⁺ dysregulation in neurons from transgenic mice expressing mutant presenilin 2. *Aging Cell.* **11**, 885–893 (2012).
88. Fontana, R. et al. Early hippocampal hyperexcitability in PS2APP mice: role of mutant PS2 and APP. *Neurobiol. Aging* **50**, 64–76 (2017).
89. Pendin, D. et al. Familial Alzheimer's disease presenilin-2 mutants affect Ca²⁺ homeostasis and brain network excitability. *Aging Clin. Exp. Res.* **33**, 1705–1708 (2021).
90. Leparulo, A. et al. Dampened Slow Oscillation Connectivity Anticipates Amyloid Deposition in the PS2APP Mouse Model of Alzheimer's Disease. *Cells* **9**, 1–20 (2019).
91. Beckman, M. et al. Loss of presenilin 2 age-dependently alters susceptibility to acute seizures and kindling acquisition. *Neurobiol. Dis.* **136**, 104719 (2020).
92. Knox, K. M., Beckman, M., Smith, C. L., Jayadev, S., Barker-haliski, M. Chronic seizures induce sex-specific cognitive deficits with loss of presenilin 2 function. *Exp. Neurol.* **361**, 114321 (2023).
93. Jarosz-Griffiths, H. H., Noble, E., Rushworth, J. V. & Hooper, N. M. Amyloid- β receptors: The good, the bad, and the prion protein. *J. Biol. Chem.* **291**, 3174–3183 (2016).

94. Verret, L. et al. Inhibitory interneuron deficit links altered network activity and cognitive dysfunction in Alzheimer model. *Cell* **149**, 708–721 (2012).
95. Palop, J. J. & Mucke, L. Network abnormalities and interneuron dysfunction in Alzheimer disease. *Nat. Rev. Neurosci.* **17**, 777–792 (2016).
96. Li, S. et al. Soluble Oligomers of Amyloid β Protein Facilitate Hippocampal Long-Term Depression by Disrupting Neuronal Glutamate Uptake. *Neuron* **62**, 788–801 (2009).
97. Li, S. et al. Soluble β oligomers inhibit long-term potentiation through a mechanism involving excessive activation of extrasynaptic NR2B-containing NMDA receptors. *J. Neurosci.* **31**, 6627–6638 (2011).
98. Zott, B. et al. A vicious cycle of β amyloid-dependent neuronal hyperactivation. *Science* **365**, 559–565 (2019).
99. Spellman, T. et al. Hippocampal-prefrontal input supports spatial encoding in working memory. *Nature* **522**, 309–314 (2015).
100. Song, D. et al. The lateralization of left hippocampal CA3 during the retrieval of spatial working memory. *Nat. Commun.* **11**, 1–13 (2020).
101. Yassa, M. A. et al. Pattern separation deficits associated with increased hippocampal CA3 and dentate gyrus activity in nondemented older adults. *Hippocampus* **21**, 968–979 (2011).
102. Zhang, C. et al. Presenilins are essential for regulating neurotransmitter release. *Nature* **460**, 632–636 (2009).
103. Zhang, D. et al. Inactivation of presenilins causes pre-synaptic impairment prior to post-synaptic dysfunction. *J. Neurochem.* **115**, 1215–1221 (2010).
104. Wu, B., Yamaguchi, H., Lai, F. A. & Shen, J. Presenilins regulate calcium homeostasis and presynaptic function via ryanodine receptors in hippocampal neurons. *Proc. Natl Acad. Sci. USA* **110**, 15091–15096 (2013).
105. Lee, S. H. et al. Presenilins regulate synaptic plasticity and mitochondrial calcium homeostasis in the hippocampal mossy fiber pathway. *Mol. Neurodegener.* **12**, 1–15 (2017).
106. Ripoli, C. et al. Intracellular accumulation of amyloid- β (A β) protein plays a major role in A β -induced alterations of glutamatergic synaptic transmission and plasticity. *J. Neurosci.* **34**, 12893–12903 (2014).
107. Zhang, H. et al. Role of A β in Alzheimer's-related synaptic dysfunction. *Front Cell Dev. Biol.* **10**, 1–14 (2022).
108. Tu, S., Okamoto S ichi, Lipton SA, Xu H. Oligomeric A β -induced synaptic dysfunction in Alzheimer's disease. *Mol. Neurodegener.* **9**, 48 (2014).
109. Woodruff, G. et al. Defective Transcytosis of APP and Lipoproteins in Human iPSC-Derived Neurons with Familial Alzheimer's Disease Mutations. *Cell Rep.* **17**, 759–773 (2016).
110. Hung, C. O. Y. & Livesey, F. J. Altered γ -Secretase Processing of APP Disrupts Lysosome and Autophagosome Function in Monogenic Alzheimer's Disease. *Cell Rep.* **25**, 3647–3660.e2 (2018).
111. Neely, K. M., Green, K. N. & LaFerla, F. M. Presenilin is necessary for efficient proteolysis through the autophagy-lysosome system in a γ -secretase-independent manner. *J. Neurosci.* **31**, 2781–2791 (2011).
112. Sambri, I. et al. Lysosomal dysfunction disrupts presynaptic maintenance and restoration of presynaptic function prevents neurodegeneration in lysosomal storage diseases. *EMBO Mol. Med.* **9**, 112–132 (2017).
113. Pará, C. et al. Early defects in mucopolysaccharidosis type IIIC disrupt excitatory synaptic transmission. *JCI Insight* **9**, 6 (2021).
114. Nemani, V. M. et al. Increased Expression of α -Synuclein Reduces Neurotransmitter Release by Inhibiting Synaptic Vesicle Reclustering after Endocytosis. *Neuron* **65**, 66–79 (2010).
115. Padamsey, Z. et al. Activity-Dependent Exocytosis of Lysosomes Regulates the Structural Plasticity of Dendritic Spines. *Neuron* **93**, 132–146 (2017).
116. Foster, W. J. et al. Hippocampal mGluR1-dependent long-term potentiation requires NAADP-mediated acidic store Ca^{2+} signaling. *Sci Signal.* **11**, eaat9093 (2018).
117. Sun, J. et al. LAMTOR1 inhibition of TRPML1-dependent lysosomal calcium release regulates dendritic lysosome trafficking and hippocampal neuronal function. *EMBO J.* **41**, 1–25 (2022).
118. Özkan, N. et al. ER – lysosome contacts at a pre-axonal region regulate axonal lysosome availability. *Nat. Commun.* **12**, 1–18 (2021).
119. Fernández-Monreal, M., Brown, T. C., Royo, M. & Esteban, J. A. The balance between receptor recycling and trafficking toward lysosomes determines synaptic strength during long-term depression. *J. Neurosci.* **32**, 13200–13205 (2012).
120. Kim, T., Yamamoto, Y., Tanaka-Yamamoto, K. Timely regulated sorting from early to late endosomes is required to maintain cerebellar long-term depression. *Nat Commun.* **8**, 1–16 (2017).
121. Yap, C. C., Digilio, L., McMahon, L. P., Garcia, A. D. R. & Winckler, B. Degradation of dendritic cargos requires Rab7-dependent transport to somatic lysosomes. *J. Cell Biol.* **217**, 3141–3159 (2018).
122. Cogli, L., Piro, F. & Bucci, C. Rab7 and the CMT2B disease. *Biochem. Soc. Trans.* **37**, 1027–1031 (2009).
123. Braggin, J. E. et al. Alternative splicing in a presenilin 2 variant associated with Alzheimer disease. *Ann. Clin. Transl. Neurol.* **6**, 762–777 (2019).
124. Course, M. M. et al. Aberrant splicing of PSEN2, but not PSEN1, in individuals with sporadic Alzheimer's disease. *Brain* **146**, 507–518 (2023).
125. Serneels, L. et al. Modeling the β -secretase cleavage site and humanizing amyloid-beta precursor protein in rat and mouse to study Alzheimer's disease. *Mol. Neurodegener.* **1**, 15 (2020).
126. Jayadev, S. et al. Presenilin 2 is the predominant γ -Secretase in microglia and modulates cytokine release. *PLoS One.* **5**, e15743 (2010).
127. Fung, S. et al. Early-Onset Familial Alzheimer Disease Variant PSEN2 N141I Heterozygosity is Associated with Altered Microglia Phenotype. *J. Alzheimer's Dis.* **77**, 675–688 (2020).
128. Nam, H. et al. Presenilin 2 N141I mutation induces hyperactive immune response through the epigenetic repression of REV-ERB α . *Nat. Commun.* **13**, 1–18 (2022).
129. Hou, P. et al. The γ -secretase substrate proteome and its role in cell signaling regulation. *Mol. Cell.* **83**, 4106–4122 (2023).
130. Van Acker, Z. P. et al. Phospholipase D3 degrades mitochondrial DNA to regulate nucleotide signaling and APP metabolism. *Nat. Commun.* **1**, 14 (2023).
131. Belevich, I., Joensuu, M., Kumar, D., Vihinen, H. & Jokitalo, E. Microscopy Image Browser: A Platform for Segmentation and Analysis of Multidimensional Datasets. *PLoS Biol.* **14**, 1–13 (2016).
132. Naert, A., Callaerts-Vegh, Z. & D'Hooge, R. Nocturnal hyperactivity, increased social novelty preference and delayed extinction of fear responses in post-weaning socially isolated mice. *Brain Res Bull.* **85**, 354–362 (2011).
133. Callaerts-Vegh, Z. et al. Concomitant deficits in working memory and fear extinction are functionally dissociated from reduced anxiety in metabotropic glutamate receptor 7-deficient mice. *J. Neurosci.* **26**, 6573–6582 (2006).

Acknowledgements

This work was financed through VIB, KU Leuven (C14/21/095 and SMINF KA/20/085 to WA), the Research Foundation – Flanders (FWO; GOC4220N and IO01322N to W.A. and G008023N to LCG), SAO-FRA (#2020/030 and 2022/022 to WA), BrightFocus (A2024033S to WA) and the Alzheimer Association (AARF-20-677499 to ZPVA and AARF-23-1149740 to CV). AP and SGF are recipients of FWO SB-strategic mandates (1S35019N and 1S59621N, respectively); ZPVA and CV are recipients of FWO postdoctoral fellowships (1250425 N and 12B7423N,

respectively). We thank T. Saido and B. De Strooper for providing the APPKI mice, J. de Wit and R. Mancuso for critical reading, N. Gunko for EM support and T. Pattenuzzo for help with TEM quantifications. The VIB BioImaging Core is acknowledged for providing access and support to confocal and EM. Figure 8 was created with Biorender (<https://www.biorender.com/>).

Author contributions

A.P. designed, performed and analysed most experiments, prepared all manuscript figures. A.P. and W.A. wrote the article with input from all other authors. Z.V.A., R.S., C.V., and A.V. contributed with primary cultures, imaging experiments on primary neurons and quantitative analysis. I.V. carried out TEM imaging and Z.V.C. coordinated the behavioral tests and contributed with A.P. to data interpretations. S.G.F. and L.C.G. contributed with MSD ELISA experiments. L.S. performed injections into the pronucleus of C57Bl6J embryos by microinjection (MutaMouse facility) for the generation of the new mouse line. E.C., B.D., and K.W. performed electrophysiological experiments. W.A. designed the overall research strategy and supervised the experiments.

Competing interests

The authors declare no competing interests.

Additional information

Supplementary information The online version contains supplementary material available at <https://doi.org/10.1038/s41467-024-54777-y>.

Correspondence and requests for materials should be addressed to Wim Annaert.

Peer review information *Nature Communications* thanks Fabien Delerue and the other, anonymous, reviewers for their contribution to the peer review of this work. A peer review file is available.

Reprints and permissions information is available at <http://www.nature.com/reprints>

Publisher's note Springer Nature remains neutral with regard to jurisdictional claims in published maps and institutional affiliations.

Open Access This article is licensed under a Creative Commons Attribution-NonCommercial-NoDerivatives 4.0 International License, which permits any non-commercial use, sharing, distribution and reproduction in any medium or format, as long as you give appropriate credit to the original author(s) and the source, provide a link to the Creative Commons licence, and indicate if you modified the licensed material. You do not have permission under this licence to share adapted material derived from this article or parts of it. The images or other third party material in this article are included in the article's Creative Commons licence, unless indicated otherwise in a credit line to the material. If material is not included in the article's Creative Commons licence and your intended use is not permitted by statutory regulation or exceeds the permitted use, you will need to obtain permission directly from the copyright holder. To view a copy of this licence, visit <http://creativecommons.org/licenses/by-nc-nd/4.0/>.

© The Author(s) 2024